Journal of Pharmaceutical Analysis 15 (2025) 101106

Contents lists available at ScienceDirect

Journal of Pharmaceutical Analysis

journal homepage: www.elsevier.com/locate/jpa

Original article

Targeting ceramide-induced microglial pyroptosis: Icariin is a promising therapy for Alzheimer's disease

Hongli Li [a, b], Qiao Xiao [a, b], Lemei Zhu [a, b], Jin Kang [c], Qiong Zhan [d, e, **], Weijun Peng [a, b, *]

[a] Department of Integrated Traditional Chinese & Western Medicine, The Second Xiangya Hospital of Central South University, Changsha, 410011, China
[b] National Clinical Research Center for Metabolic Diseases, Changsha, 410011, China
[c] Department of Rheumatology and Immunology, The Second Xiangya Hospital of Central South University, Changsha, 410011, China
[d] Department of Neurology, The Second Xiangya Hospital of Central South University, Changsha, 410011, China
[e] Clinical Medical Research Center for Stroke Prevention and Treatment of Hunan Province, Department of Neurology, The Second Xiangya Hospital of Central South University, Changsha, 410011, China

ARTICLE INFO

Article history:
Received 16 May 2024
Received in revised form
3 September 2024
Accepted 13 September 2024
Available online 19 September 2024

Keywords:
Alzheimer's disease
Ceramides
Microglia pyroptosis
COX2
NLRP3 inflammasome
Icariin

ABSTRACT

Alzheimer's disease (AD), a progressive dementia, is one of the most common neurodegenerative diseases. Clinical trial results of amyloid-β (Aβ) and tau regulators based on the pretext of straightforward amyloid and tau immunotherapy were disappointing. There are currently no effective strategies for slowing the progression of AD. Herein, we spotlight the dysregulation of lipid metabolism, particularly the elevation of ceramides (Cers), as a critical yet underexplored facet of AD pathogenesis. Our study delineates the role of Cers in promoting microglial pyroptosis, a form of programmed cell death distinct from apoptosis and necroptosis, characterized by cellular swelling, and membrane rupture mediated by the NLRP3 inflammasome pathway. Utilizing both *in vivo* experiments with amyloid precursor protein (APP)/presenilin 1 (PS1) transgenic mice and *in vitro* assays with BV-2 microglial cells, we investigate the activation of microglial pyroptosis by Cers and its inhibition by icariin (ICA), a flavonoid with known antioxidant and anti-inflammatory properties. Our findings reveal a significant increase in Cers levels and pyroptosis markers (NOD-like receptor family, pyrin domain containing 3 (NLRP3), apoptosis-associated speck-like protein containing a caspase recruitment domain, caspase-1, gasdermin D (gasdermin D (GSDMD)), and interleukin-18 (IL-18)) in the brains of AD model mice, indicating a direct involvement of Cers in AD pathology through the induction of microglial pyroptosis. Conversely, ICA treatment effectively reduces these pyroptotic markers and Cer levels, thereby attenuating microglial pyroptosis and suggesting a novel therapeutic mechanism of action against AD. This study not only advances our understanding of the pathogenic role of Cers in AD but also introduces ICA as a promising candidate for AD therapy, capable of mitigating neuroinflammation and pyroptosis through the cyclooxygenase-2 (COX-2)-NLRP3 inflammasome-gasdermin D (GSDMD) axis. Our results pave the way for further exploration of Cer metabolism disorders in neurodegenerative diseases and highlight the therapeutic potential of targeting microglial pyroptosis in AD.

1. Introduction

Alzheimer's disease (AD), the most common form of dementia, is a neurodegenerative disorder characterized by the accumulation of β-amyloid (Aβ) plaques and the formation of neurofibrillary tangles in the brain [1]. AD primarily manifests as a progressive deterioration of cognitive functions and memory loss, and has become a major public health challenge [2]. Although the pathogenesis of AD is not fully elucidated, microglia are thought to be a central part of the cellular response in AD pathogenesis [3].

Microglia are resident immune surveillance cells of the central nervous system (CNS) and have been the focus of extensive research due to their diverse biological activities [4]. In normal physiological states, the activation of microglia can effectively eliminate invading pathogens and secrete neurotrophic factors to regulate the stability of the microenvironment. While under pathological conditions, over-activated microglia secrete numerous

---

* Corresponding author. Department of Integrated Traditional Chinese & Western Medicine, The Second Xiangya Hospital of Central South University, Changsha, 410011, China.

** Corresponding author. Department of Neurology, the Second Xiangya Hospital of Central South University, Changsha, 410011, China.

E-mail addresses: zhanqiong51@csu.edu.cn (Q. Zhan), pengweijun87@csu.edu.cn (W. Peng).

Peer review under responsibility of Xi'an Jiaotong University.

https://doi.org/10.1016/j.jpha.2024.101106

inflammatory cytokines, leading to neuroinflammation and eventually resulting in severe nerve damage [5]. Studies have also shown that overactivation and death of microglia is a major cause of AD [6]. Thus, the fate of microglia is extremely important for neuronal damage and cognitive dysfunction.

Activation of the NOD-like receptor family, pyrin domain containing 3 (NLRP3) inflammasome and the occurrence of pyroptosis in microglia are implicated in the pathogenesis of AD [7]. The NLRP3 inflammasome, a well-characterized multi-protein complex, consists of nod-like receptors (NLRs), apoptosis-associated speck-like protein containing a caspase recruitment domain (ASC), and pro-caspase-1 [8]. Upon recognizing various stimuli, NLRP3 forms complexes that activate caspase-1, which in turn triggers the cleavage of gasdermin D (GSDMD) and the precursors of interleukin-18 (IL-18) and interleukin-1β (IL-1β), leading to pyroptosis and the release of pro-inflammatory cytokines [9]. Research indicates that the NLRP3 inflammasome triggers microglial pyroptosis in AD, with GSDMD playing a key role [10]. However, the precise mechanisms of NLRP3-mediated pyroptosis in AD is still unclear.

Recent findings suggest an involvement of sphingolipid (SL) metabolism in the activation of the NLRP3 inflammasome [11]. SLs are essential for the development and maintenance of the nervous system's functional integrity [12]. Ceramides (Cers), central to SL metabolism, play a critical role in sustaining essential physiological functions such as cell death and differentiation, proliferation, cycle arrest, migration stimulation, senescence, necrosis, necroptosis, autophagy, mitophagy, and cytoskeletal rearrangement [13]. An increase in Cer levels has been observed in the brains of AD patients and animals, suggesting a significant contribution to the disease's pathology [14]. Moreover, Cers are known to activate the NLRP3 inflammasome, leading to microglial activation [15]. Additionally, Cers have been found to promote programmed cell death through a range of molecular mechanisms, including the activation of Bcl-2-associated X protein (Bax), cytochrome C, various caspases, mitogen-activated protein kinases (MAPKs), protein kinase C (PKC) isoforms, and kinase suppressor of Ras [16]. Although previous studies have predominantly shown that Cers promote programmed cell death, their role in inducing pyroptosis has been less frequently reported. Interestingly, recent studies revealed that Cer regulates pyroptosis respectively in wild-type cancer cells through the NLRP3—caspase-1—GSDMD pathway [17] and in human umbilical vein endothelial cells (HUVECs) through the thioredoxin-interacting protein (TXNIP)/NLRP3/GSDMD signaling pathway [18]. Despite these insights, the role of the elevated cerebral Cer levels in the activation of microglia pyroptosis signaling pathways in AD remains largely unexplored.

Icariin (ICA), a flavone compound extracted from *Epimedium grandiflorum*, shows a range of pharmacological effects, such as antioxidant, anti-inflammatory, and anti-aging properties [19]. In the context of AD treatment, ICA exerts its therapeutic effects through various mechanisms. Notably, our previous research has revealed that ICA may regulate sphingolipid metabolism through the protein kinase C alpha (PRKCA)/tumor necrosis factor (TNF)/tumor protein 53 (TP53)/AKT serine/threonine kinase 1 (AKT1)/v-rel reticuloendotheliosis viral oncogene homolog A (RELA)/nuclear factor kappa B subunit (NFKB1) axis for the treatment of AD [20]. Furthermore, ICA mitigates M1 activation of microglia and reduces Aβ plaque accumulation in the hippocampus and prefrontal cortex by activating peroxisome proliferator-activated receptor gamma (PPARγ) in restraint/isolation-stressed amyloid precursor protein (APP)/presenilin 1 (PS1) mice [21]. Icariin also alleviates cognitive dysfunction and astrocytic pyroptosis in hemorrhagic shock resuscitation model mice [22]. Additionally, studies have shown that ICA reduces lipopolysaccharide (LPS)-induced pyroptosis by suppressing the NLRP3 inflammasome-mediated caspase-1 signaling pathway in models of osteoarthritis [23]. While the neuroprotective effects and inhibition of pyroptosis by ICA in the central nervous system (CNS) are well documented, the specific role and mechanism of ICA in Cer-induced microglia pyroptosis remains poorly understood.

Herein, this study conducted *in vivo* experiments with APP/PS1 transgenic mice and *in vitro* studies using BV-2 microglial cells, and we seek to explore the pivotal role of Cer in promoting microglial pyroptosis and to determine whether ICA can ameliorate AD by reducing Cer levels and inhibiting Cer-induced microglial pyroptosis.

2. Materials and methods

2.1. Animals

Male C57BL/6J mice (wild type (WT)) and APP/PS1 transgenic mice were acquired from SiPeifu Biotechnology (Beijing, China). These mice were housed under controlled environmental conditions (12 h light/dark cycle at a constant temperature of 24 °C and 53% humidity). A standard laboratory diet and water was provided ad libitum. All mice underwent an acclimatization period of at least one week before the commencement of the study. The study predominantly utilized male WT mice as the control group. All procedures involving animals were conducted in strict adherence to the ethical guidelines and protocols approved by the Animal Ethics Committee of the Changsha Medical University (Approval No.: D2023020).

In the first part of the animal experiment, we used 9-month-old male C57BL/6J and APP/PS1 mice. After 7 days of adaptive feeding, these mice underwent subsequent experiments. In the second part of the animal experiment, we used 6-month-old male C57BL/6J and APP/PS1 mice. Following 7 days of adaptive feeding, the mice were randomly divided into four groups: the WT group, the APP/PS1 group, the WT + ICA group, and the APP/PS1+ICA group. Subsequently, the mice received oral gavage for 100 days. ICA was dissolved in dimethyl sulfoxide (DMSO) and then diluted with saline (final solution containing 1% DMSO) before intragastric administration. The WT + ICA group and APP/PS1 + ICA groups were orally administered with ICA at a dose of 100 mg/kg/day; the two other groups were given the same volume of sterile normal saline (solution containing 1% DMSO). The intervention dosage of ICA (100 mg/kg/day) for APP/PS1 mice was determined based on prior literature research and preliminary studies conducted by our research group [20].

2.2. Morris water maze (MWM) test

The MWM test was conducted in a circular pool filled with water, surrounded by extra-maze cues, as described in our previous study [24]. Briefly, each mouse underwent four trials daily over a span of five consecutive days, with a 15-min intertrial interval. The maximum trial duration was 60 s, and if mice did not reach the platform in the allotted time, they were manually guided to it. Following the acquisition phase, a probe trial was conducted with the platform removed to measure the time spent in the quadrant that previously contained the platform, over a period of 60 s. The Super Maze Morris system (XR-XM101, Shanghai XM Intelligent Technology Co., Ltd., Shanghai, China) was utilized to record swimming paths, escape latency, and time spent in the target quadrant.

2.3. Hematoxylin and eosin (HE) staining

HE staining was conducted according to the routine protocol. Briefly, at the end of the MWM tasks, mice were anesthetized and underwent transcardial perfusion with physiological saline solution to clear intravascular blood. Brains were subsequently extracted, fixed in 4% paraformaldehyde, embedded in paraffin, and sectioned at 4–5 μm thickness. These sections were stained with HE and examined under optical microscopy for pathological alterations.

2.4. *Transmission electron microscopy (TEM)*

The ultrastructural changes of the hippocampus were observed using TEM. In brief, brain tissues were prepared for TEM by fixing in 2.5% glutaraldehyde for 24 h, succeeded by post-fixation in 1% osmium tetroxide for 3 h. Subsequent to fixation, the samples underwent a dehydration process in gradient ethanol (50%, 70%, 90%, and 100%) for 10 min each, and were embedded in resin and cut into a thickness of 50–60 nm. The prepared sections were then subjected to staining using uranyl acetate and lead citrate, prior to their examination under a transmission electron microscope (Model HT7700, Hitachi, Tokyo, Japan).

2.5. *Immunofluorescence (IF) and immunohistochemistry (IHC) staining*

Brain samples from WT and APP/PS1 mice were fixed, embedded, and sectioned as per standardized protocols. The intact brains underwent fixation in 4% paraformaldehyde, and were subsequently embedded in paraffin, and finally sectioned into 3 μm slices. For the IF staining, the procedure comprised sequential steps: washing, permeabilization, and blocking. The brain sections were incubated with primary antibodies targeting ionized calcium binding adapter molecule 1 (IBA-1) (10904-1-AP, 1:100; Proteintech, Wuhan, China), GSDMD (20770-1-AP, 1:100; Proteintech), and ceramide (C8104, 1:50; Merck, Shanghai, China). This was followed by an incubation step with the respective fluorophore-conjugated secondary antibodies (A21206, 1:400; Life technologies, Danvers, MA, USA; ab97230, 1:1000; Abcam, Shanghai, China). 4′,6-diamidino-2-phenylindole (DAPI) staining was integrated during the concluding wash. The immunofluorescence images of the whole brain were captured using a 3DHISTECH slide scanning system (Pannoramic SCAN II, 3DHISTECH Ltd., Budapest, Hungary). Image refinement and fluorescence intensity analyses were conducted employing ImageJ and Adobe Photoshop CS. Parallel sections were designated for Aβ IHC. The preliminary stages mirrored those of immunofluorescence staining. These slices were immersed with the primary Aβ antibody (GB111197, 1:100; Servicebio, Wuhan, China) and allowed to incubate overnight at 4 °C. This was succeeded by an incubation with the secondary antibody (ab205718, 1:2000; Abcam, Shanghai, China) at room temperature for 45 min. Color visualization was achieved using diaminobenzidine (DAB). After staining, the slides were scanned using a slide scanner (NanoZoomer S360, Hamamatsu, Shizuoka, Japan).

2.6. *Cell culture and in vitro model*

Murine microglial BV-2 cells were obtained from Central South University (Changsha, China). BV-2 cells, which function similarly to primary microglia and are widely used in neurodegenerative disorder research [25]. BV-2 cells were cultured in Dulbecco's modified Eagle medium (DMEM) supplemented with 10% fetal bovine serum (FBS) and 1% penicillin/streptomycin. For the experiments, BV-2 cells were seeded in 6- or 96-well plates and allowed to adhere for 24 h before any treatment. In the preliminary experiments, the cells were treated for 13, 16 and 24 h respectively with C2-Cer (860502 P, Sigma, Shanghai, China) at different concentrations (25, 50 and 75 μM); in the other experiments, the cells were pre-treated with 10 and 20 μM of ICA respectively for 36 h and then treated with 75 μM of C2-Cer for 16 h. Untreated cells were used as control group. DMSO treated cells were used as controls of the ICA treated cells. We used the following abbreviations for the treatments: The cells treated with both ICA and Cer received the treatments sequentially, with ICA added first for pre-treatment, followed by the addition of Cer for intervention. All experiments were carried out in a humidified atmosphere containing 5% CO_2 at 37 °C.

2.7. *Cell viability assay and cell morphology*

Cell counting kit-8 (C6005, NCM Biotech, Wuhan, China) was used to determine cell viability. Briefly, BV-2 cells were seeded in a 96-well plate and treated with DMEM medium containing Cer and/or ICA. Following the treatment, the cells were incubated with cell counting kit-8 (CCK-8) working solution for 1 h. Subsequently, the OD_{450} value was measured using a microplate reader (Epoch, BioTek, Winooski, VT, USA) to quantify cell viability.

BV-2 cells were plated at 1×10^5 cells/well in 6-well plates. After being cultured 24 h, the cells were treated with Cer or treated with ICA followed by Cer. Cell morphology was evaluated using an optical microscope. Besides, to further delineate the critical role of cyclooxygenase-2 (COX-2) in Cer-induced microglial pyroptosis, we employed NS-398, a widely reported COX-2 inhibitor known for its specific inhibition of COX-2 expression [26,27], in our interventions on Cer-treated microglial cells.

2.8. *Lactate dehydrogenase (LDH) release assay*

LDH is an indicator of cell membrane integrity and is also used to indirectly indicate the onset of pyroptosis. In brief, cells were cultured in 96-well plates and then subjected to different treatments. One hour before assay, 20 μL of LDH release agent was added to the culture medium. LDH release was assayed using the Cytotoxicity Detection Kit as described by the manufacturer's protocol (C0017, Beyotime, Shanghai, China).

2.9. *Hoechst 33342 and propidium iodide (PI) staining*

To evaluate the BV-2 cell membrane integrity, Hoechst 33342 and PI double staining was performed. In short, BV-2 cells were seeded in 6-well plates and exposed to the DMEM medium supplemented with the specified agents. The cells were subsequently incubated with Hoechst 33342 (1 mg/mL) and PI (5 mg/mL) for 15 min at 37 °C. Fluorescence excitation and imaging were performed using a Nikon TS2R-FL microscope (Nikon, Tokyo, Japan).

2.10. *Data acquisition and analysis for Cer metabolism genes in human brain*

Our investigation into the genes regulating Cer metabolism was derived from two publicly accessible platforms. Data were obtained from the Seattle Alzheimer's Disease Cell Atlas (https://sea-ad.org; syn26223298) and the CZ CELLxGENE Discover data platform (cellxgene.cziscience.com) [28]. For the visualization, we utilized the ABC Atlas tool, part of the Allen Brain Cell Atlas (https://portal.brain-map.org/atlases-and-data/bkp/abc-atlas;RRID:SCR_024440). All procedures were performed in accordance with the guidelines provided on the websites for analysis and data download.

2.11. *RNA-seq analysis*

BV-2 cells were seeded onto sterile 150 mm × 15 mm Petri dish for grown for 24 h and then pre-treated with ICA for 36 h before

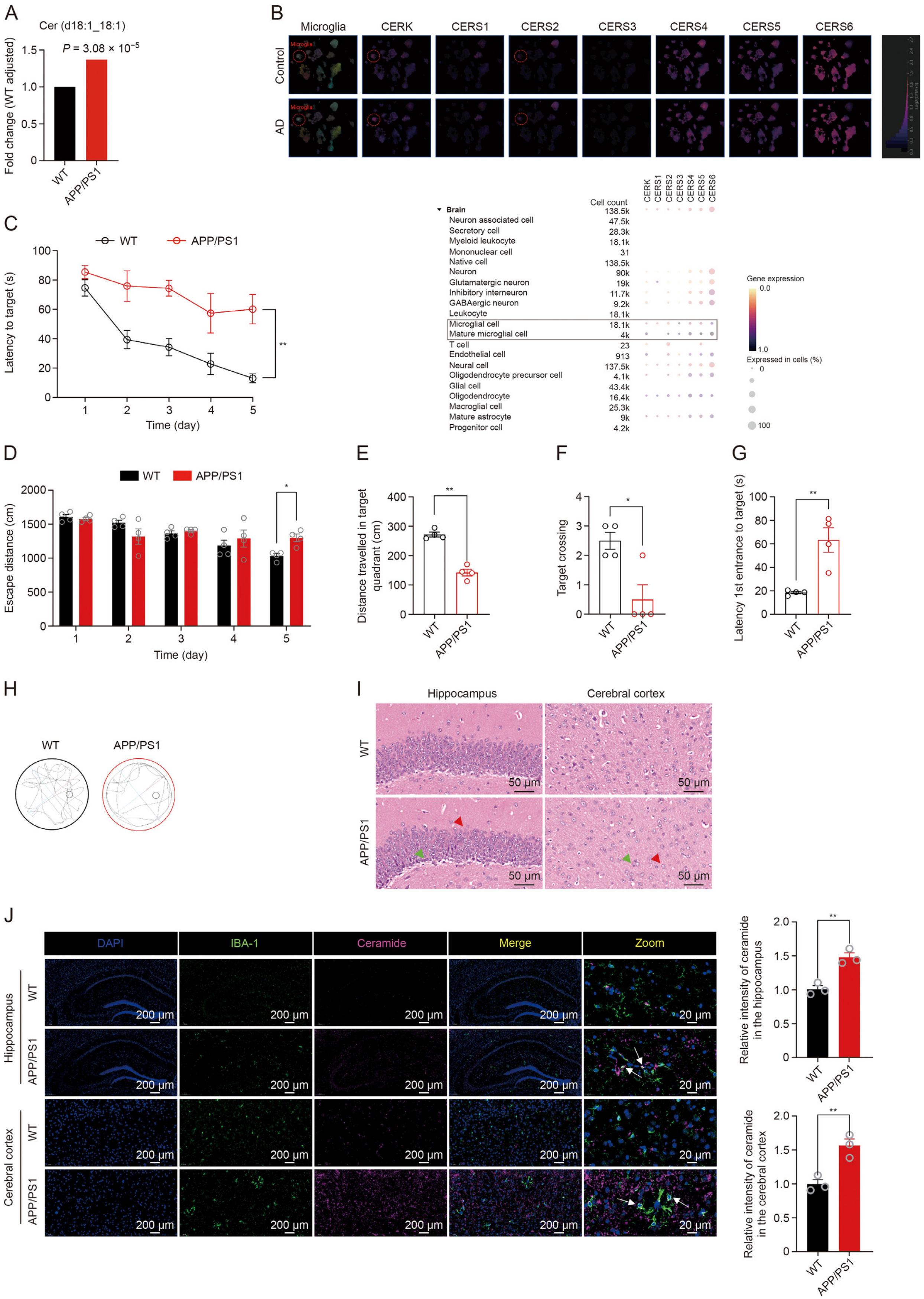
A
Cer (d18:1_18:1)
P = 3.08 × 10−5
Fold change (WT adjusted)
WT
APP/PS1
B
Microglia
CERK
CERS1
CERS2
CERS3
CERS4
CERS5
CERS6
Control
AD
Brain
Cell count
Neuron associated cell 138.5k
Secretory cell 47.5k
Myeloid leukocyte 28.3k
Mononuclear cell 18.1k
Native cell 31
Neuron 138.5k
Glutamatergic neuron 90k
Inhibitory interneuron 19k
GABAergic neuron 11.7k
Leukocyte 9.2k
Microglial cell 18.1k
Mature microglial cell 18.1k
T cell 4k
Endothelial cell 23
Neural cell 913
Oligodendrocyte precursor cell 137.5k
Glial cell 4.1k
Oligodendrocyte 43.4k
Macroglial cell 16.4k
Mature astrocyte 25.3k
Progenitor cell 9k
4.2k
Gene expression
0.0
1.0
Expressed in cells (%)
0
100
C
WT
APP/PS1
Latency to target (s)
Time (day)
**
D
WT
APP/PS1
Escape distance (cm)
Time (day)
*
E
Distance travelled in target quadrant (cm)
**
F
Target crossing
*
G
Latency 1st entrance to target (s)
**
H
WT
APP/PS1
I
Hippocampus
Cerebral cortex
WT
APP/PS1
50 μm
J
DAPI
IBA-1
Ceramide
Merge
Zoom
Hippocampus
Cerebral cortex
WT
APP/PS1
200 μm
20 μm
Relative intensity of ceramide in the hippocampus
Relative intensity of ceramide in the cerebral cortex
**

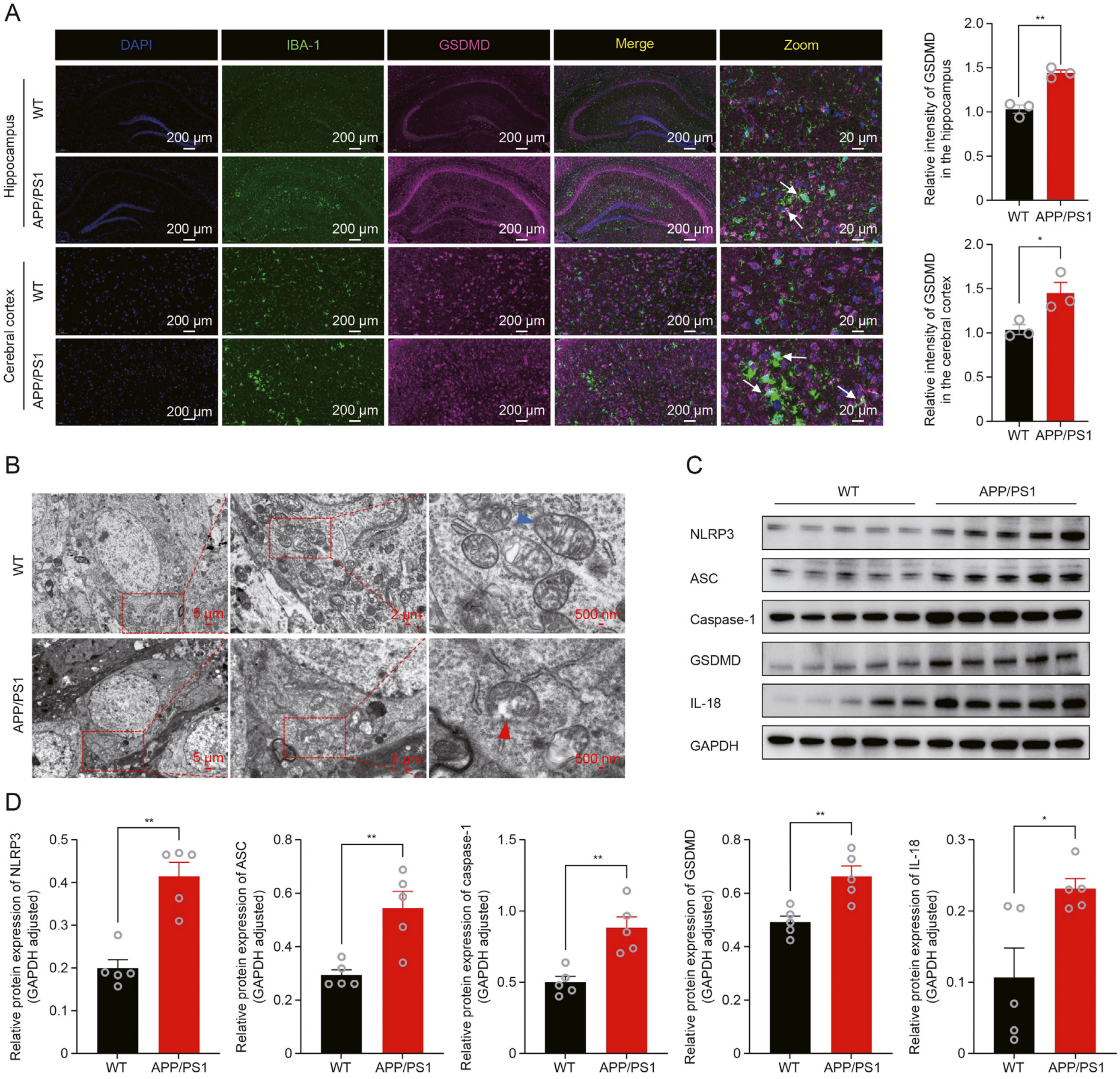

Fig. 2. Microglial pyroptosis in amyloid precursor protein (APP)/presenilin 1 (PS1) mice. (A) Representative immunofluorescent staining of gasdermin D (GSDMD) and ionized calcium-binding adaptor molecule 1 (IBA-1) in the brain of APP/PS1 and wild type (WT) mice. Higher magnification images are presented (hippocampus: two-tailed unpaired *t*-test: $t = 7.048$, *d.f.* $= 4$, $P = 0.0021$; cerebral cortex: two-tailed unpaired *t*-test: $t = 3.103$, *d.f.* $= 4$, $P = 0.0361$). (B) Representative transmission electron microscopy (TEM) images showing morphological changes of mitochondria. Higher magnification images are presented. Blue arrows indicating normal mitochondrial morphology, and red arrows indicating abnormal mitochondrial morphology, including rounded mitochondria, swelling, and blurred cristae. (C) The protein expression of NOD-like receptor family, pyrin domain containing 3 (NLRP3), apoptosis-associated speck-like protein containing a caspase recruitment domain (ASC), caspase-1, GSDMD and interleukin-18 (IL-18) in hippocampus was detected by Western blot assays. (D) Quantitative analysis of Western blot (NLRP3: two-tailed unpaired *t*-test: $t = 5.594$, *d.f.* $= 8$, $P = 0.0005$; ASC: $t = 3.850$, *d.f.* $= 8$, $P = 0.0049$; caspase-1: $t = 4.234$, *d.f.* $= 8$, $P = 0.0029$; GSDMD: $t = 3.761$, *d.f.* $= 8$, $P = 0.0055$; IL-18: $t = 2.861$, *d.f.* $= 8$, $P = 0.0211$). $^{*}P < 0.05$, $^{**}P < 0.01$ versus WT group. DAPI: 4′,6-diamidino-2-phenylindole; GAPDH: glyceraldehyde-3-phosphate dehydrogenase.

Fig. 1. Elevated ceramide (Cer) levels in amyloid precursor protein (APP)/presenilin 1 (PS1) mice. (A) Cer levels in the brains of APP/PS1 mice. (B) Uniform manifold approximation and projection (UMAP) plot of expression distribution of genes involved in Cer metabolism in single-nucleus RNA sequencing data from the Seattle Alzheimer's Disease Cell Atlas (upper panel, sourced from public database data on the human brain). Darker colors indicate higher expression levels, with red circles indicating microglial cells. Heatmap of the genes involved in Cer metabolism (lower panel, sourced from public database data on the human brain). (C, D) The escape latency (C) and escape distance (D) during acquisition phase of the morris water maze (MWM) test (escape latency: two-way analysis of variance (ANOVA), interaction between time and group, $F(4,24) = 2.942$, $P = 0.0412$; effect of group, $F(1,6) = 16.57$, $P = 0.0066$; escape distance: two-way ANOVA, interaction between time and group, $F(4,24) = 3.527$, $P = 0.0212$; effect of group, $F(1,6) = 0.5932$, $P = 0.0469$). (E−G) The distance travelled in the target quadrant (E) (two-tailed unpaired *t*-test: $t = 3.464$, *d.f.* $= 6$, $P = 0.0134$), number of platform crossings (F) (two-tailed unpaired *t*-test: $t = 9.094$, *d.f.* $= 6$, $P < 0.0001$), and the latency 1st entrance to target (G) (two-tailed unpaired *t*-test: $t = 4.265$, *d.f.* $= 6$, $P = 0.0053$) in the probe trial of the MWM test on day 6. (H) Representative swimming trails of the two groups. (I) Representative images of hematoxylin and eosin (HE) staining in the brain of APP/PS1 and wild type (WT) mice. The green arrows indicate pyknosis, and the red arrows signify obscured nuclear boundaries and increased cytoplasm. (J) Representative immunofluorescent staining of Cer and ionized calcium binding adapter molecule 1 (IBA-1) in the brain of APP/PS1 and WT mice. Higher magnification images are presented (hippocampus: two-tailed unpaired *t*-test: $t = 5.733$, *d.f.* $= 4$, $P = 0.0046$; cerebral cortex: two-tailed unpaired *t*-test: $t = 4.780$, *d.f.* $= 4$, $P = 0.0088$). $^{*}P < 0.05$, $^{**}P < 0.01$ versus WT group. AD: Alzheimer's disease; CERK: ceramide kinase; DAPI: 4′,6-diamidino-2-phenylindole.

treated with Cer for 16 h. After treatment, total RNAs were isolated from cells with Trizol reagent (15596026, Invitrogen, Carlsbad, CA, USA), and the sequencing libraries were prepared. Poly-A-containing mRNA was isolated from the total RNA using poly-T oligo-attached magnetic beads and then fragmented by an RNA fragmentation kit. The cDNA was synthesized through reverse transcription, employing random primers. After the ligation with the adaptor, the cDNA was amplified by 15 cycles of polymerase chain reaction (PCR). Subsequently, 200-bp cDNA fragments were isolated via gel electrophoresis. RNA sequencing was conducted on the Illumina HiSeq 2500 platform by Shanghai Majorbio Biopharm Technology (Shanghai, China). Data analysis was performed on the free online platform of Majorbio Cloud Platform (www.majorbio.com). The differential expression of genes was selected by a fold change (FC) of >2 and *P* adjust <0.05.

2.12. Western blotting

Cells and brain tissue were washed with ice-cold PBS and subsequently lysed using radio-immunoprecipitation assay (RIPA) lysis buffer supplemented with a protease inhibitor cocktail, maintained at 4 °C for 30 min, followed by centrifugation at 15,000 rpm for 25 min. The supernatant collected was then denatured by boiling in loading buffer. After sodium dodecyl sulfate-polyacrylamide gel electrophoresis (SDS-PAGE), the separated proteins were transferred to a polyvinylidene difluoride (PVDF) membrane. The membrane was blocked using tris buffered saline (TBS) supplemented with 5% non-fat milk and 0.1% Tween 20 (TBST) at room temperature for 2 h. It was then incubated overnight at 4 °C with primary antibodies against NLRP3 (ab263899,1: 1000; Abcam), ASC (67824s, 1:1000; Cell Signaling Technology, Danvers, MA, USA), caspase-1 (24232s, 1:1000; Cell Signaling Technology), GSDMD (20770-1-AP, 1:100; Proteintech), IL-18 (ab207323, 1: 1000; Abcam), COX-2 (27308-1-AP, 1:500; Proteintech), and glyceraldehyde-3-phosphate dehydrogenase (GAPDH) (10494-1-AP, 1:5000; Proteintech). Following primary antibody incubation, membranes were exposed to appropriate secondary antibodies at room temperature for 2 h, then washed with TBST. Detection was performed using an enhanced chemiluminescence system (Bio-Rad, ChemiDoc, Hercules, CA, USA).

2.13. Molecular docking

A semi-flexible docking approach was adopted for this study as previously reported [29]. The 2D structure of ICA was obtained from the PubChem database (PubChem CID: 5318997), and the 3D crystal structures of PTGS2 (PDB code: 5F1A and 3LN1) were downloaded from the Research Collaboratory for Structural Bioinformatics (RCSB) Protein Data Bank (PDB) database (https://www.rcsb.org/). Preparation of the protein structures for docking involved the removal of all non-receptor atoms, including water molecules, ions, and miscellaneous compounds, using Discover Studio Visualizer. The irrelevant ligands present in the crystal structure were removed to ensure the single-chain receptor protein was optimally prepared for docking, utilizing AutoDock Tools (Version 1.5.6) for this preparatory phase. The prepared receptor protein then was used for molecular docking with the active ligand component via AutoDock Vina (version 1.2.0). The docking process was calculated by the genetic algorithm. All docking runs adhered to the default parameter settings. After docking, ligands of the lowest binding energy were selected for detailed visualization of the ligand—protein interactions using PyMOL (version 3.0).

2.14. Molecular dynamics simulation

Molecular dynamics simulations were performed using the GROMACS 2022 software package, for the receptor protein with the highest binding energy to the ligand molecule in the molecular docking results to obtain its binding mode and binding energy to the ligand. The simulations commenced with the molecular docking results serving as the initial structure configuration. The process began with energy minimization to ensure the system was in its lowest possible energy state, followed by a brief phase of molecular dynamics simulation under vacuum conditions for 100 ps. Both the Coulomb force intercept and van der Waals radius intercept were 1.4 nm. Subsequently, the system was equilibrated using the regular system (NVT) and isothermal isobaric system (NPT), and then molecular dynamics simulations were performed for 100 ns at room temperature and pressure.

2.15. Cellular thermal shift assay (CETSA)

The direct binding of ICA to its target was validated using CETSA. BV-2 cells were incubated with or without 20 μM ICA for 2.5 h. The treated cells were harvested and resuspended in phosphate-buffered saline. Cell suspensions were aliquoted into seven PCR tubes, each subjected to a specific temperature (38, 42, 46, 50, 54, 58, and 62 °C) for 3 min, followed by a stabilization period at 25 °C for 3 min. Cell lysis was achieved through three freeze-thaw cycles. After centrifugation at 20,000 *g* for 10 min, the soluble fractions were analyzed by Western blotting. The subsequent steps for Western blotting, including the preparation of samples, SDS-PAGE, protein transfer to PVDF membranes, blocking, antibody incubation, and signal detection, were performed following the same protocol described in the previous Western blotting experiment.

2.16. Statistical analysis

Data were presented as mean ± standard error of the mean (SEM) and were processed using GraphPad Prism 9.5.0 for statistical evaluation. Statistical significance was determined by using Student's *t*-test or Wilcoxon matched-pairs signed rank test. One-way analysis of variance (ANOVA) or two-way ANOVA was performed in multiple experimental groups. *P*-value <0.05 was deemed statistically significant.

3. Results

3.1. Elevated Cer levels and concurrent microglial pyroptosis in APP/PS1 mice

In this study, an elevation in Cer levels was observed in the brains of APP/PS1 mice when compared with WT mice (Fig. 1A) [30]. Besides, an analysis of single-nucleus RNA sequencing data from the Seattle Alzheimer's Disease Cell Atlas and single-cell RNA sequencing data from CZ CellxGene Discover data platform [28] revealed that genes involved in Cer metabolism are significantly upregulated in the microglia of AD patients compared with controls (Fig. 1B). These findings highlight the potential role of Cer dysregulation in the progression of AD.

To advance our understanding of Cer's role in AD pathology, we conducted a comprehensive study on APP/PS1 and WT mice. The MWM test revealed cognitive impairments in APP/PS1 mice, as indicated by increased escape latencies, longer escape distances, decreased distances travelled in target quadrant, fewer platform crossings, and increased latency for the first entrance to the target

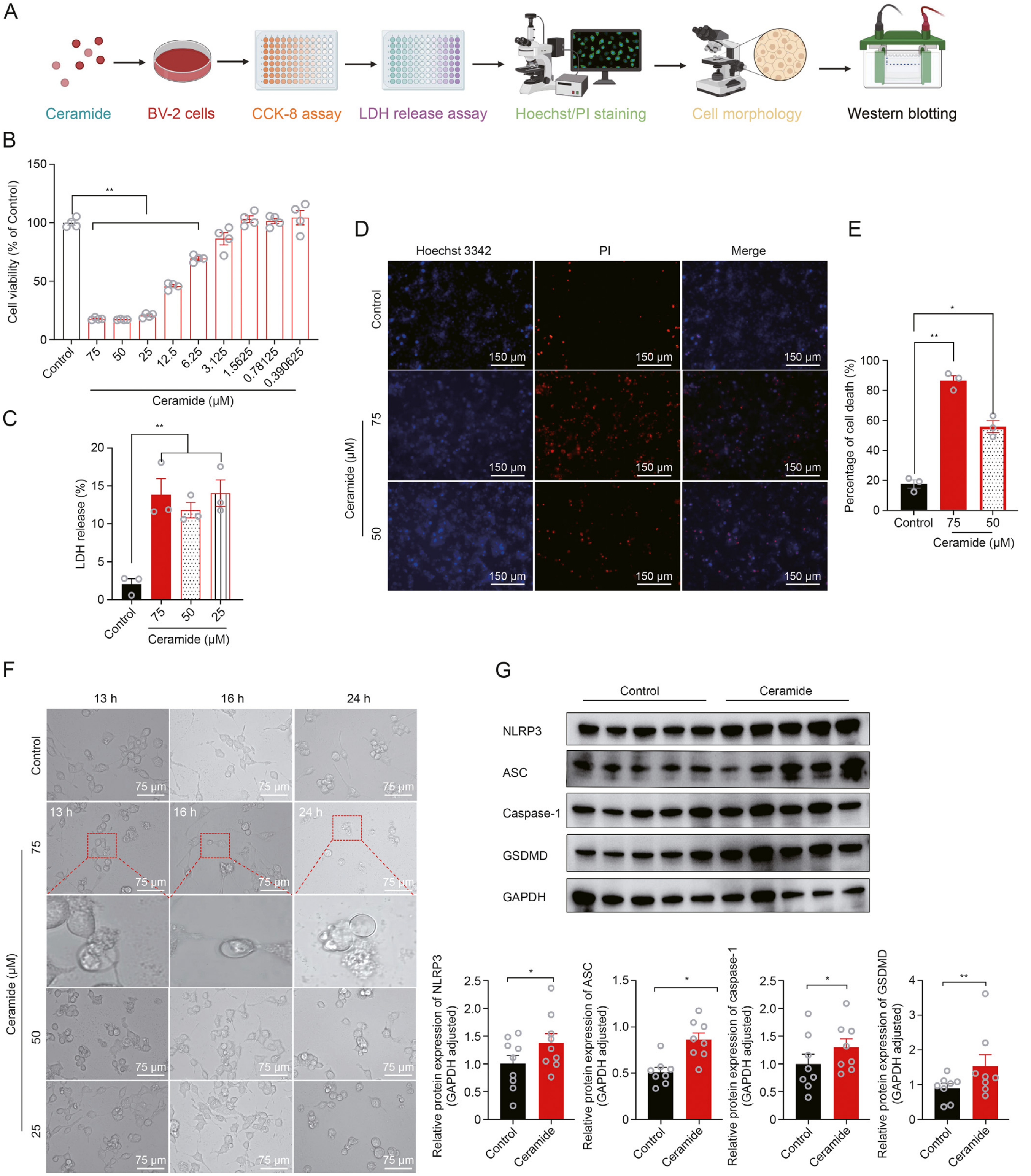

Fig. 3. Ceramide (Cer) induces pyroptosis in BV-2 microglial cells. (A) Schematic diagram illustrating Cer treatment leading to microglial pyroptosis. (B) Cell viability was assessed by the cell counting kit-8 (CCK-8) assay (one-way analysis of variance (ANOVA), $F\,(9, 30) = 3.113$, $P < 0.0001$; Dunnett's multiple comparisons: Control versus 75, $P < 0.0001$; Control versus 50, $P < 0.0001$; Control versus 25, $P = 0.014$; Control versus 12.5, $P < 0.0001$; Control versus 6.25, $P < 0.0001$; Control versus 3.125, $P = 0.0203$). (C–E) Cell membrane integrity was assessed by lactate dehydrogenase (LDH) release assay (one-way ANOVA, $F\,(2, 6) = 0.1357$, $P < 0.0001$; Dunnett's multiple comparisons: Control versus 75, $P = 0.0015$; Control versus 50, $P = 0.0049$; Control versus 25, $P = 0.014$) (C) and Hoechst/propidium iodide (PI) staining (D, E) (one-way analysis of variance (ANOVA), $F\,(3, 8) = 0.2482$, $P = 0.0015$; Dunnett's multiple comparisons: Control versus 75, $P < 0.0001$; Control versus 50, $P = 0.0004$). (F) Cell morphology changes assessed by light microscopy. The bottom image represents a magnified view (× 5.25) of the area marked by the red box in the top image. (G) The protein expression of NOD-like receptor family, pyrin domain containing 3 (NLRP3), apoptosis-associated speck-like protein containing a caspase recruitment domain (ASC), caspase-1, and gasdermin D (GSDMD) in BV-2 microglia was detected by Western blot assays (NLRP3: two-tailed paired t-test: $t = 2.451$, $d.f. = 8$, $P = 0.0399$; ASC: $t = 4.182$, $d.f. = 4$, $P = 0.0139$; caspase-1: $t = 2.437$, $d.f. = 7$, $P = 0.0449$; GSDMD: Wilcoxon matched-pairs signed rank test: $P = 0.0078$). $^{*}P < 0.05$, $^{**}P < 0.01$ versus Control group. GAPDH: glyceraldehyde-3-phosphate dehydrogenase.

compared with WT controls (Figs. 1C–H). HE staining of brain sections showed decreased cellular density, disrupted cellular arrangement, and notable pyknosis, hyperemia, and swelling in APP/PS1 mice 1 (Fig. 1I). Additionally, IF staining of Cer in the hippocampus and cortex revealed significant Cer upregulation, coinciding with microglial activation in APP/PS1 mice relative to WT controls (Fig. 1J).

Given the established role of microglial pyroptosis in AD and the reported capacity of Cer to induce this form of cell death, we conducted preliminary *in vivo* experiments to investigate whether increased Cer levels are associated with the occurrence of microglial pyroptosis. IF staining for GSDMD and the microglial marker IBA-1 validated the presence of pyroptosis in microglia, with significantly increased GSDMD fluorescence intensity compared with WT mice (Fig. 2A). Through TEM, we observed pronounced mitochondrial morphological changes in APP/PS1 mice, including small globular mitochondria with marked swelling structure, collapse cristae, and disruption of membranes, internal structural disorder, and swelling global structure. Whereas mitochondria in WT mice exhibited long tubular or short virgulate shapes with clear cristae ridges (Fig. 2B). Western blot assays showed elevated NLRP3, ASC, caspase-1, GSDMD, and IL-18 levels in the hippocampus of APP/PS1 mice versus WT controls (Figs. 2C and D). Collectively, these findings preliminarily suggest a potentially pivotal role of Cer in promoting microglial pyroptosis in APP/PS1 mice.

3.2. *Cer may induce microglial pyroptosis via regulating COX-2 in vitro experiments*

To further investigate whether Cer can induce microglial pyroptosis, we conducted *in vitro* experiments using Cer-treated BV-2 microglial cells. The experimental workflow was exhibited

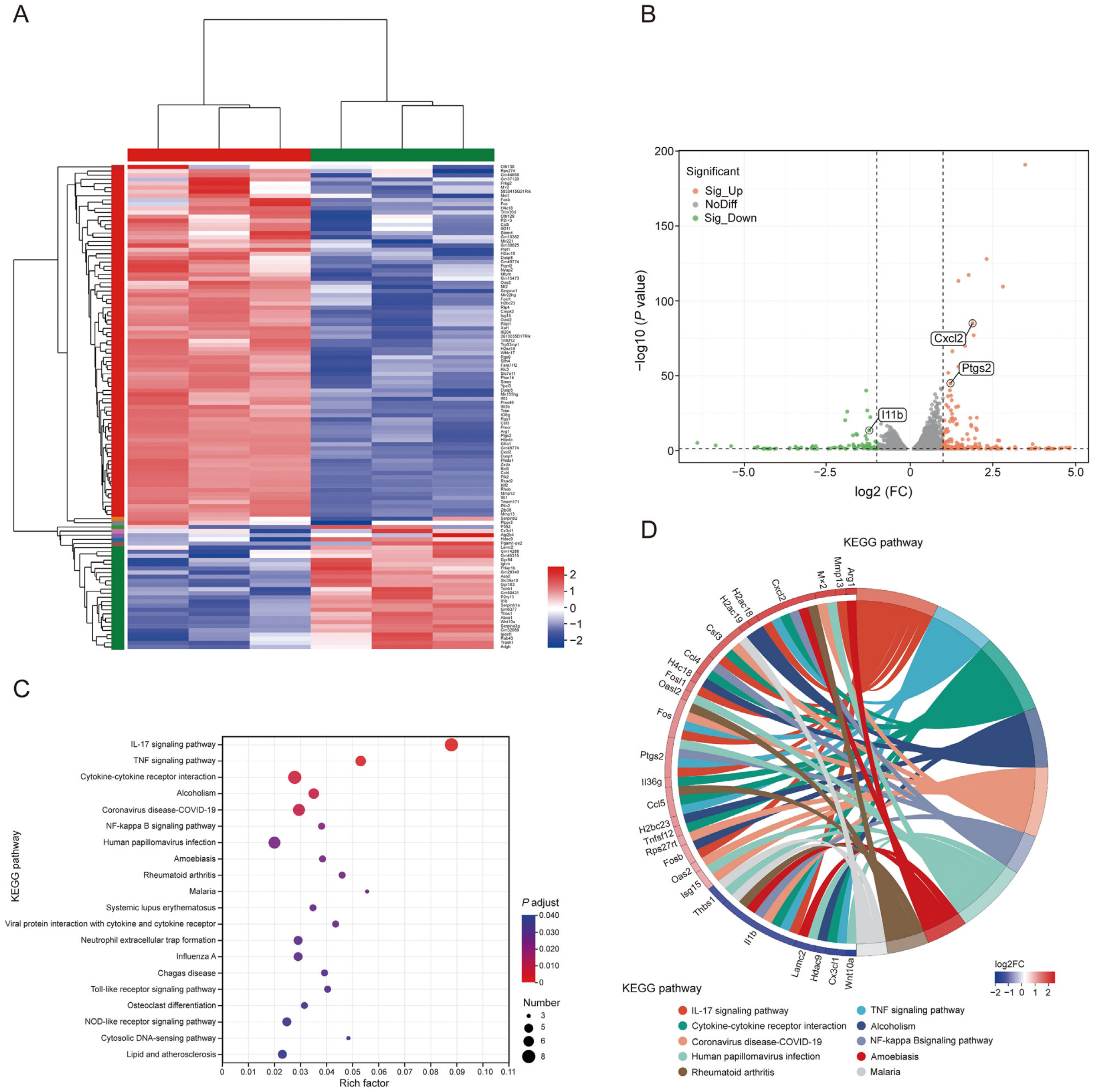

Fig. 4. Ceramide (Cer) may induce BV-2 microglial cell pyroptosis by upregulating cyclooxygenase-2 (COX-2). (A, B) Heatmap (A) and volcano plot (B) of differentially expressed genes detected in BV-2 microglial cells after Cer treatment. (C) Kyoto Encyclopedia of Genes and Genomes (KEGG) pathway enrichment of differentially expressed genes. (D) Circular pathway diagram illustrating the relationship between pathways and genes. Unpaired Student's *t*-test was used for statistical analysis. $n = 3–5$ per group.

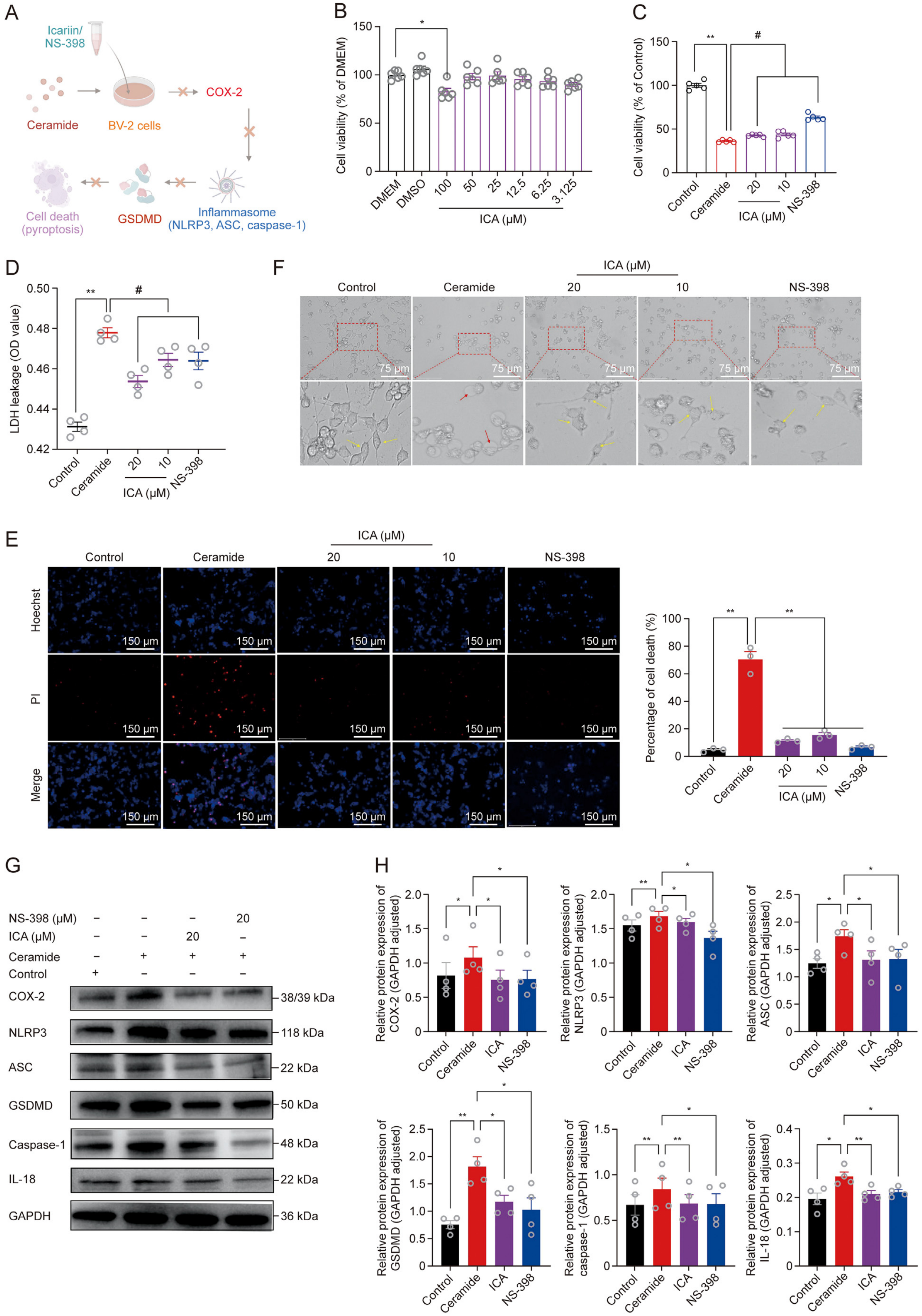
A
Icariin/ NS-398
Ceramide
BV-2 cells
COX-2
Inflammasome (NLRP3, ASC, caspase-1)
GSDMD
Cell death (pyroptosis)
B
Cell viability (% of DMEM)
150
100
50
0
DMEM
DMSO
100
50
25
12.5
6.25
3.125
ICA (μM)
*
C
Cell viability (% of Control)
150
100
50
0
Control
Ceramide
20
10
NS-398
ICA (μM)
**
#
D
LDH leakage (OD value)
0.50
0.48
0.46
0.44
0.42
Control
Ceramide
20
10
NS-398
ICA (μM)
**
#
F
ICA (μM)
Control
Ceramide
20
10
NS-398
75 μm
E
ICA (μM)
Control
Ceramide
20
10
NS-398
Hoechst
PI
Merge
150 μm
Percentage of cell death (%)
100
80
60
40
20
0
Control
Ceramide
20
10
NS-398
ICA (μM)
**
**
G
NS-398 (μM) – – – 20
ICA (μM) – – 20 –
Ceramide – + + +
Control + – – –
COX-2 38/39 kDa
NLRP3 118 kDa
ASC 22 kDa
GSDMD 50 kDa
Caspase-1 48 kDa
IL-18 22 kDa
GAPDH 36 kDa
H
Relative protein expression of COX-2 (GAPDH adjusted)
Relative protein expression of NLRP3 (GAPDH adjusted)
Relative protein expression of ASC (GAPDH adjusted)
Relative protein expression of GSDMD (GAPDH adjusted)
Relative protein expression of caspase-1 (GAPDH adjusted)
Relative protein expression of IL-18 (GAPDH adjusted)
Control
Ceramide
ICA
NS-398
*
**

as in Fig. 3A. First, to investigate the effect of Cer on the viability of microglial cells, cells were treated with varying concentrations of Cer (6.25, 12.5, 25, 50, and 75 μM), and a CCK-8 assay was conducted to assess cytotoxic effects. The results showed that treatment with Cer at all concentrations significantly reduced the viability of BV-2 cells compared with the control group, as depicted in Fig. 3B. Subsequently, the LDH release assay and Hoechst/PI staining were performed, aiming to identify the mode of cell death, including apoptosis, pyroptosis, or necroptosis. Consistently, the Cer-treated groups exhibited increased LDH release and a higher number of PI-positive cells, as shown in Figs. 3C–E. These findings suggest enhanced cell membrane rupture. To further delineate the specific mode of cell death induced by Cer, we observed morphological changes in BV-2 cells after Cer treatment. Optical microscopy examination (Fig. 3F) revealed significant morphological alterations; Cer-treated BV-2 cells displayed swelling, rupture, and bubble-like protrusions indicative of pyroptotic bodies. In contrast, cells in the control group exhibited an inactivated, dendritic, resting state typical of microglia. Western blot analysis corroborated these observations, showing that Cer exposure markedly elevated the protein levels of critical pyroptosis markers, including NLRP3, ASC, caspase-1, and GSDMD (Fig. 3G). Collectively, these results strongly suggest that Cer triggers pyroptosis in microglial cells.

To further clarify the mechanism underlying Cer-induced pyroptosis in microglial cells, transcriptome sequencing was performed on BV-2 cells post-Cer treatment (Fig. 4). The transcriptomic analysis identified 117 differentially expressed genes in Cer-treated BV-2 cells compared with the control group, with 87 genes being upregulated and 30 downregulated ($|FC| > 2$, adjust $P < 0.05$) (Figs. 4A and B). Kyoto Encyclopedia of Genes and Genomes (KEGG) pathway enrichment analysis highlighted significant alterations in pathways, including interleukin 17 (IL-17) signaling, tumor necrosis factor (TNF) signaling, and nuclear factor kappa B (NF-κB) signaling pathways, implicating genes such as PTGS2 (COX-2), IL-1β, and Cxcl2 (Figs. 4C and D). Given the pivotal roles these genes assume in driving inflammatory responses, an extensive review of the literature guided our focus towards COX-2, attributed to its critical function in inflammation modulation and its proposed role in NLRP3 inflammasome activation. Our findings revealed a potential mechanism by which Cer may induce microglial pyroptosis through the upregulation of COX-2.

3.3. ICA may inhibit Cer-induced microglial pyroptosis by targeting COX-2

Experimental workflow for further delineating the critical role of COX-2 in Cer-induced microglial pyroptosis was depicted in Fig. 5A. Initially, we investigate the inhibitory effect of ICA on Cer-induced microglial pyroptosis. As indicated in Fig. 5B, ICA treatment at concentrations of 50 μM or lower had no effect on the viability of BV-2 cells compared with control group. This confirms that these concentrations of ICA are non-toxic and suitable for further experiments. Next, cell viability was assessed using CCK-8 assays, showing that cell viability significantly decreased in the Cer-treated group compared with the control group. However, pre-treatment with ICA for 36 h ameliorated the decrease in cell viability induced by Cer (Fig. 5C). This indicates that ICA has a protective effect against Cer-induced cytotoxicity in BV-2 cells. Additionally, LDH release experiments showed a significant increase in LDH release in the Cer-treated group, which was significantly reduced in the ICA treated groups (Fig. 5D). Hoechst/PI staining results revealed an increase in red fluorescence in the Cer-treated group, but this was significantly reduced in the ICA treated groups (Fig. 5E). Microscopic observations showed that Cer treatment led to typical pyroptotic changes in BV-2 cells, which was noticeably attenuated by ICA pretreatment (Fig. 5F). Western Blot results showed that the expression levels of COX-2, NLRP3, ASC, GSDMD, caspase-1, and IL-18 proteins were significantly increased in the Cer-treated group, but significantly decreased in the ICA treated groups (Figs. 5G and H).

Meanwhile, to further delineate the critical role of COX-2 in Cer-induced microglial pyroptosis, we employed NS-398, a widely reported COX-2 inhibitor known for its specific inhibition of COX-2 expression, in our interventions on Cer-treated microglial cells. The CCK-8 assays showed that cell viability significantly decreased in the Cer-treated group compared with the control group. However, pre-treatment with NS-398 for 36 h ameliorated the decrease in cell viability induced by Cer (Fig. 5C). Additionally, LDH release experiments (Fig. 5D) indicated a significant increase in LDH release in the Cer-treated group, which was significantly reduced in the NS-398 treated groups. Hoechst/PI staining results (Fig. 5F) demonstrated an increase in red fluorescence in the Cer-treated group, indicating cell membrane rupture, which was significantly reduced in the NS-398 treated groups. Collectively, the LDH release assay and Hoechst/PI staining indicated that NS-398 significantly reduced Cer-induced cell membrane rupture and pyroptosis. Microscopic observations (Fig. 5E) revealed that Cer treatment led to typical pyroptotic changes in BV-2 cells, including cell swelling, membrane rupture, and bubble-like pyroptotic bodies, which was noticeably attenuated by NS-398 pretreatment. Western Blot results (Figs. 5G and H) showed that the expression levels of COX-2, NLRP3, ASC, GSDMD, caspase-1, and IL-18 proteins were significantly increased in the Cer-treated group, but significantly decreased in the NS-398 treated groups. In conclusion, our results indicate that ICA may act as a potential COX-2 inhibitor, effectively suppressing microglial pyroptosis induced by Cer.

To further elucidate the interaction between ICA and COX-2, we conducted 3D molecular docking and molecular dynamics

Fig. 5. Icariin (ICA) and NS-398 alleviate ceramide (Cer)-induced pyroptosis in BV-2 microglial cells. (A) Schematic representation illustrating the protective role of ICA and NS-398 against Cer-induced pyroptosis in BV-2 microglial cells. (B) Cell viability of BV-2 microglial cells evaluated via the cell counting kit-8 (CCK-8) assay to determine non-toxic dosage of ICA on BV-2 microglial cells (one-way analysis of variance (ANOVA), $F(7, 40) = 0.1995$, $P < 0.0001$; Dunnett's multiple comparisons, DMEM versus 100, $P = 0.0010$). (C) Assessment of BV-2 cell viability using the CCK-8 assay, examining the effects of NS-398 and ICA on Cer-treated BV-2 cells (one-way ANOVA, $F(4, 20) = 1.253$, $P < 0.0001$; Dunnett's multiple comparisons, Ceramide versus Control, $P < 0.0001$; Ceramide versus 20, $P = 0.0203$; Ceramide versus 10, $P = 0.0058$; Ceramide versus NS-398, $P < 0.0001$). (D) Analysis of cell membrane integrity through the lactate dehydrogenase (LDH) release assay (one-way ANOVA, $F(4, 15) = 0.6154$, $P < 0.0001$; Dunnett's multiple comparisons: Ceramide versus Control, $P < 0.0001$; Ceramide versus 20, $P < 0.0001$; Ceramide versus 10, $P < 0.0001$; Ceramide versus NS-398, $P < 0.0001$). (E) Hoechst/propidium iodide (PI) staining to evaluate cell membrane integrity (One-way ANOVA, $F(4, 10) = 1.628$, $P < 0.0001$; Dunnett's multiple comparisons: Ceramide versus Control, $P < 0.0001$; Ceramide versus 20, $P < 0.0001$; Ceramide versus 10, $P < 0.0001$; Ceramide versus NS-398, $P < 0.0001$). Observation of cellular morphological alterations via light microscopy. (F) Observation of cellular morphological alterations via light microscopy. The bottom image represents a magnified view (× 3) of the area marked by the red box in the top image. (G) The protein expression of inflammatory and pyroptosis-associated proteins (cyclooxygenase-2 (COX-2), NOD-like receptor family, pyrin domain containing 3 (NLRP3), apoptosis-associated speck-like protein containing a caspase recruitment domain (ASC), gasdermin D (GSDMD), caspase-1, and interleukin-18 (IL-18)) in BV-2 microglia was detected by Western blot assays. (H) Quantitative analysis of Western blot (one-way ANOVA with Dunnett's multiple comparisons: Ceramide versus Control, $P = 0.0401$ (COX-2), $P = 0.0030$ (NLRP3), $P = 0.0359$ (ASC), $P = 0.0088$ (GSDMD), $P = 0.0056$ (caspase-1), $P = 0.0209$ (IL-18); Ceramide versus ICA, $P = 0.0244$ (COX-2), $P = 0.0390$ (NLRP3), $P = 0.0479$ (ASC), $P = 0.0229$ (GSDMD), $P = 0.0087$ (caspase-1), $P = 0.0022$ (IL-18); Ceramide versus NS-398, $P = 0.0114$ (COX-2), $P = 0.0333$ (NLRP3), $P = 0.0259$ (ASC), $P = 0.0279$ (GSDMD), $P = 0.0218$ (caspase-1), $P = 0.0157$ (IL-18)). $^{\#}P < 0.05$, $^{*}P < 0.05$, $^{**}P < 0.01$ versus Ceramide group. OD: optical density; DMEM: Dulbecco's modified Eagle medium; DMSO: dimethyl sulfoxide; GAPDH: glyceraldehyde-3-phosphate dehydrogenase.

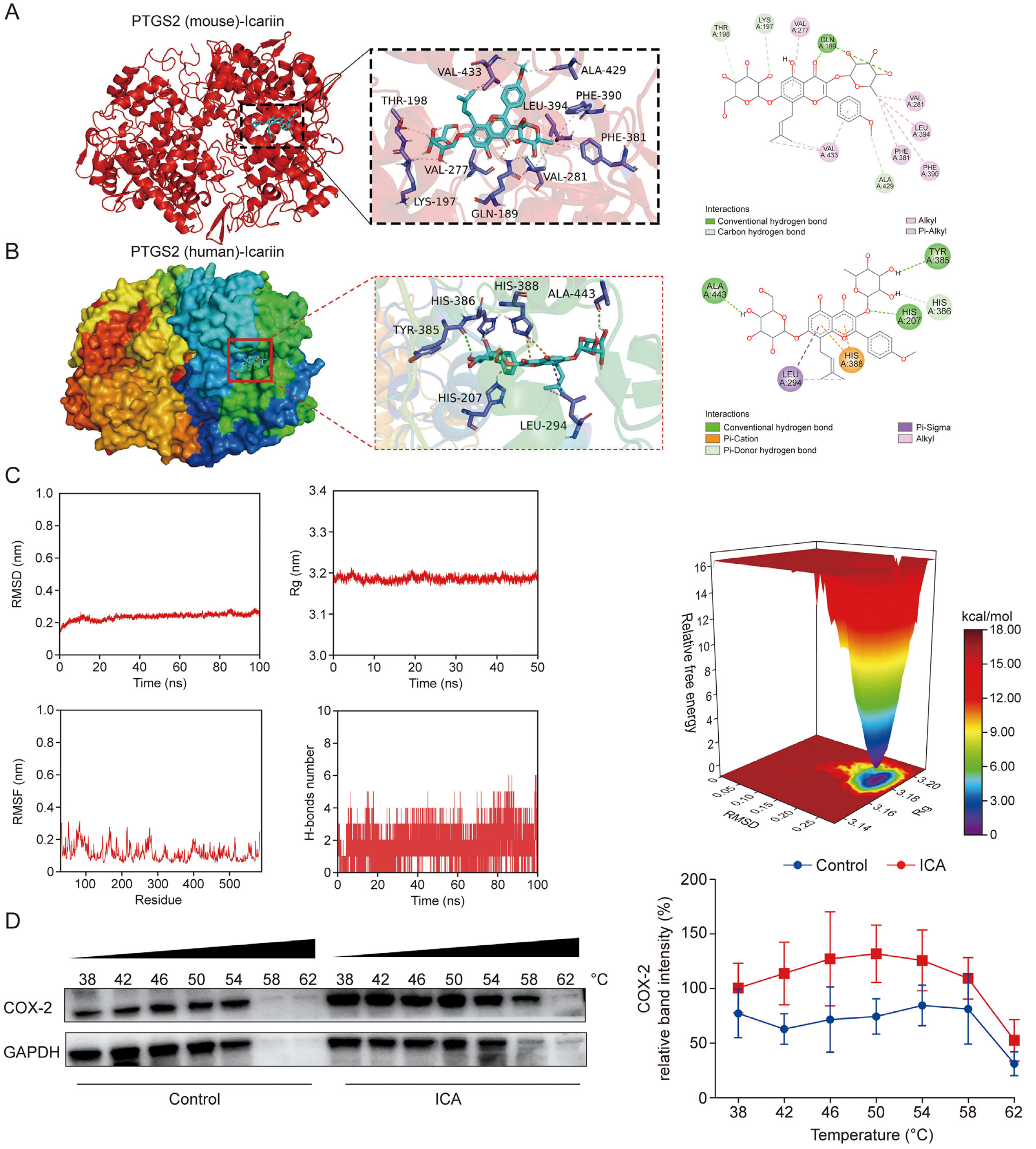

Fig. 6. Icariin (ICA) may inhibit microglial pyroptosis by targeting cyclooxygenase-2 (COX-2). (A, B) 3D molecular docking analysis of ICA (blue) and COX-2 (mouse: red; human: multicolored). (C) Molecular dynamics simulations demonstrating the strong binding affinity between ICA and COX-2. The root mean square deviation (RMSD) curve provides an indicator of the stability of the protein-ligand complex, with a smoother RMSD curve indicating higher stability; The root mean square fluctuation (RMSF) curve represents the extent of fluctuations of amino acid residues throughout the simulation, with higher RMSF values indicating greater fluctuations and vice versa; The radius of gyration (Rg) measures the compactness and stability of the structure, with larger Rg values indicating significant expansion and lower values suggesting a more compact and stable system during the simulation; The number of stabilizing H-bonds between the ligand and protein at the binding site is quantified; The free energy landscape (FEL) depicts the conformations with the lowest energy throughout the dynamic simulation process. A weak or unstable interaction between the protein and ligand is indicated by the presence of multiple, rough energy minima clusters, whereas a strong and stable interaction is characterized by nearly single, smooth energy clusters. (D) Cellular thermal shift assay (CETSA) experiment confirmed the binding capability of ICA to COX-2. One-way analysis of variance (ANOVA) was used for statistical analysis followed by Tukey's multiple comparisons test. GAPDH: glyceraldehyde-3-phosphate dehydrogenase.

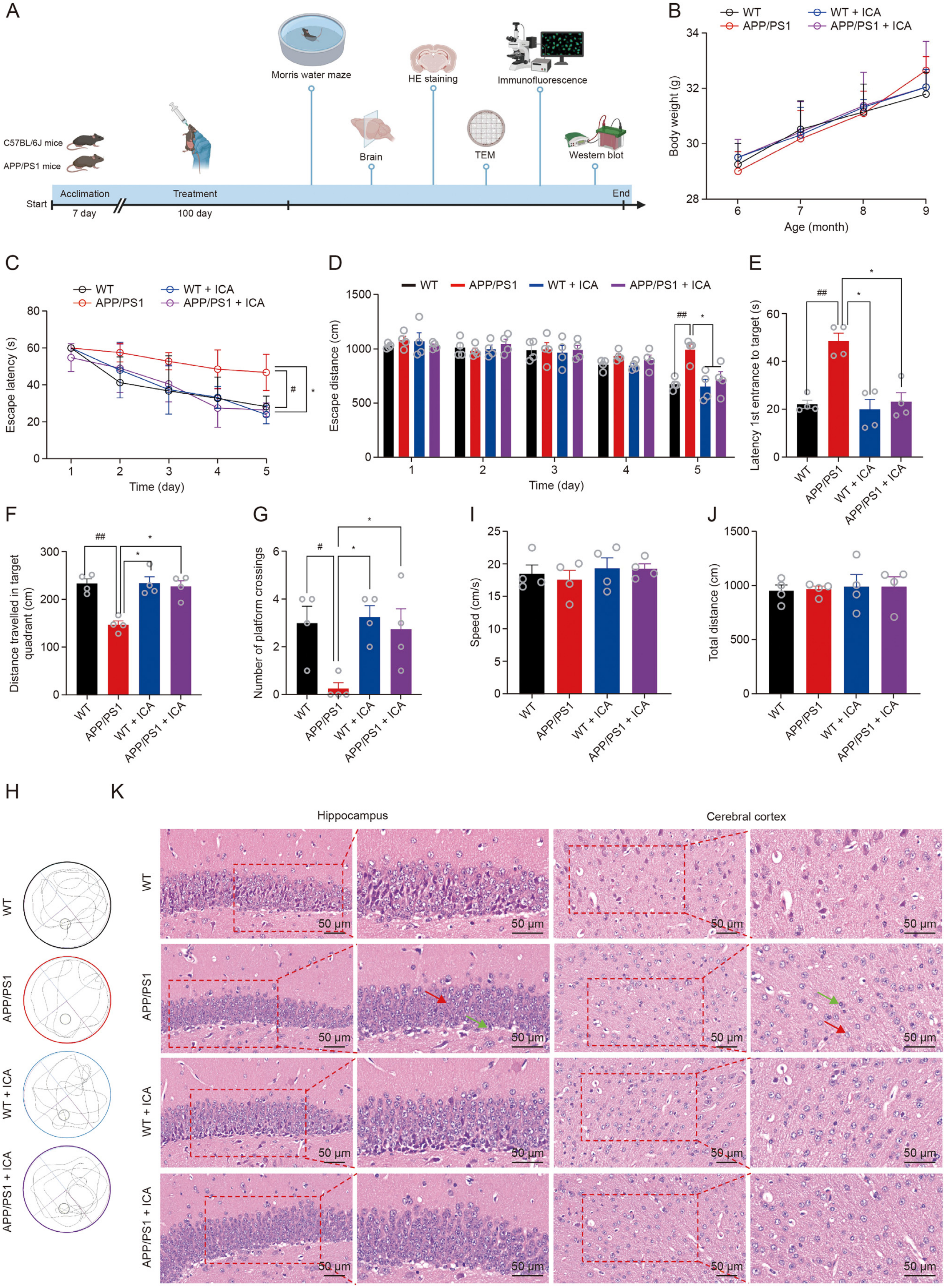

Fig. 7. Icariin (ICA) improves cognitive dysfunction in amyloid precursor protein (APP)/presenilin 1 (PS1) mice. (A) Schematic diagram of the oral administration of ICA to APP/PS1 mice, observing changes in animal cognitive function and the inhibitory effect on microglial pyroptosis. (B) The body weight (Two-way analysis of variance (ANOVA) with repeated

simulations, alongside CETSA assay. The 3D molecular docking results (Figs. 6A and B) indicated a strong binding affinity between ICA and the COX-2 receptor protein, displaying significant binding energies in both mouse (−8.2 kcal/mol) and human COX-2 proteins (−8.2 kcal/mol), all indicative of robust binding. The molecular dynamics simulations (Fig. 6C) confirmed the stability of the ICA-COX-2 complex, with root mean square deviation (RMSD) fluctuations within 0.5 nm, achieving stability after 10 ns without significant deviations. This stability indicates a highly stable structure of the ICA-COX-2 complex. The root mean square fluctuation (RMSF) and radius of gyration (Rg) analyses further corroborated the minimal impact of ICA on the amino acid residues' stability, underscoring the complex's robustness. The hydrogen bond (H-bond) analysis revealed a stable number of hydrogen bonds throughout the simulation, with peaks up to six bonds, highlighting the hydrophilic interaction strength between ICA and COX-2. The free energy landscape (FEL) analysis depicted a singular minimal energy cluster, emphasizing the complex's stability. CETSA confirmed ICA's binding to COX-2, enhancing its thermal stability and indicating a reduction in COX-2 degradation from 38 to 62 °C in the ICA group (Fig. 6D). These results imply that ICA may slow down the thermal degradation of COX-2 via directly binding to it. In summary, our findings suggest that ICA may exerts its inhibitory effects on microglia pyroptosis by specifically targeting COX-2.

3.4. ICA may attenuate AD pathology by reducing Cer levels and inhibiting Cer-induced microglial pyroptosis

To explore the therapeutic potential of ICA in inhibiting microglial pyroptosis in AD, we conducted studies in APP/PS1 transgenic mice. The experimental workflow is illustrated in Fig. 7A. Initially, we measured the body weight changes of the mice in each group throughout the experiment. The results indicated that ICA administration did not significantly affect the body weight of the mice compared to the WT or APP/PS1 groups (Fig. 7B). Subsequently, the MWM tests were performed to assess cognitive functions. As shown in Figs. 7C−G and H, APP/PS1 mice exhibited prolonged escape latency, increased escape distance and latency for the first entrance to the target, decreased distance travelled in the target quadrant, and reduced platform crossings compared with WT mice and WT + ICA mice. Notably, following ICA treatment, these cognitive impairments of APP/PS1 mice were significantly ameliorated. However, there were no differences in the swimming speed and total swimming distance among the groups (Figs. 7I and J). HE staining indicated the disorganized and damaged cellular structures observed in APP/PS1 mice, which was alleviated by ICA treatment (Fig. 7K). IHC results showed that Aβ plaque deposition was significantly pronounced in APP/PS1 mice but was reduced following ICA treatment (Fig. 8A). IF staining revealed that ICA treatment reduced Cer expression in the hippocampus and cortex of APP/PS1 mice (Fig. 8B). Furthermore, IF staining for GSDMD and IBA-1 indicated an increase in pyroptosis in APP/PS1 mice, which was attenuated by ICA treatment (Fig. 9A). TEM results indicated the disorganized and damaged cellular structures observed in APP/PS1 mice, which was alleviated by ICA treatment (Fig. 9B). Western blot analysis further confirmed the significant downregulation of COX-2, NLRP3, GSDMD, ASC, caspase-1, and IL-18 expression levels in the ICA-treated group compared with APP/PS1 mice (Figs. 9C and D). In summary, our findings underscore the therapeutic potential of ICA for AD treatment, primarily through reducing cerebral Cer levels and downregulating the COX2 expression levels, thereby inhibiting microglial pyroptosis.

4. Discussion

To the best of our knowledge, this study is the first to delineate the pathogenic effects of Cers on AD and elucidate its underlying molecular mechanisms, establishing that ICA can exert therapeutic effects against AD by targeting Cers. Specifically, we found that in APP/PS1 mice, cognitive impairments were observed alongside increased levels of Cers and enhanced microglial pyroptosis. Additionally, elevated Cer levels could trigger COX-2 activation, subsequently leading to NLRP3 inflammasome/GSDMD-induced microglial pyroptosis. ICA emerged as a promising therapeutic agent against AD by alleviating microglial pyroptosis through reducing Cer levels and regulating the COX2-NLRP3 inflammasome-GSDMD pathway. This study is unique in that it specifically addresses these mechanisms in the context of AD, providing new insights into the role of Cers and the potential therapeutic effects of ICA in this neurodegenerative disease. The schematic diagram of our findings is illustrated in Fig. 10.

Pyroptosis is recognized as a pro-inflammatory form of programmed cell death, initiated by the assembly of inflammasome, leading to cell lysis and the release of pro-inflammatory cytokines [31]. This process involves numerous molecules and regulates multiple signaling pathways, including the classical, non-classical, caspase-3-dependent, and caspase-8-dependent pathways [32]. In the classical pathway, NLRP3 inflammasome are activated. This activation converts pro-caspase-1 into caspase-1, which then cleaves the full-length GSDMD into GSDMD-N and GSDMD-C. GSDMD-N oligomerizes and boosts cell membrane pore formation by binding to membranes and destroying the membrane stability [33]. Studies have indicated that pyroptosis in microglia is predominantly mediated by this classical pathway [34]. Specifically, recent research on AD highlighted the detection of NLRP3 inflammasome and cleaved GSDMD in microglial cells within the human AD brain [10]. Consistently, our investigation demonstrated elevated levels of NLRP3 inflammasome components (ASC, NLRP3, and caspase-1) and pyroptosis-related proteins (cleaved GSDMD and IL-18) in the microglia of APP/PS1 mice brain and Cer-treated BV2 microglia, reinforcing the critical role of this pathway in AD pathology. Additionally, from our IF staining results, we observed that the number of GSDMD-positive cells was significantly higher than the number of microglia, suggesting the occurrence of pyroptosis in other cell types within the AD brain. A recent study confirmed this finding, showing the activation of the pyroptosis pathway in microglia, astrocytes, and neurons, via distinct cell

measures: interaction between time and group, $F(9, 36) = 0.08049$, $P = 0.9998$; effect of group, $F(3,12) = 0.02690$, $P = 0.9937$). (C, D) The escape latency (C) and escape distance (D) during acquisition phase of morris water maze (MWM test) (escape latency: two-way ANOVA with repeated measures, interaction between time and group, $F(12, 48) = 0.9392$, $P = 0.5172$; effect of time, $F(2.826, 33.91) = 21.91$, $P < 0.0001$; effect of group, $F(3, 12) = 7.058$, $P = 0.0055$; escape distance: two-way ANOVA with repeated measures: interaction between time and group, $F(12, 48) = 2.264$, $P = 0.0228$; effect of group, $F(3, 12) = 7.058$, $P = 0.0363$). (E−G) The latency 1st entrance to the target (E), the distance travelled in the target quadrant (F) and the number of platform crossings (G) in the probe trial of the MWM test (entrance to the target: one-way ANOVA, $F(3, 12) = 1.825$, $P = 0.0002$; Tukey's multiple comparisons test, APP/PS1 versus wild type (WT), $P = 0.0006$; WT versus WT + ICA, $P = 0.9704$; APP/PS1 versus APP/PS1 + ICA, $P = 0.0009$; the distance travelled in the target quadrant: $F(3, 12) = 0.2397$, $P = 0.0003$; APP/PS1 versus WT, $P = 0.0007$; WT versus WT + ICA, $P = 0.9999$; APP/PS1 versus APP/PS1 + ICA, $P = 0.0013$; the number of platform crossings: $F(3, 12) = 1.207$, $P = 0.0169$; APP/PS1 versus WT, $P = 0.0363$; WT versus WT + ICA, $P = 0.9914$; APP/PS1 versus APP/PS1 + ICA, $P = 0.0469$). (H) Representative swimming trails of three groups. (I) Swimming speed (one-way ANOVA, $F(3, 12) = 0.9075$, $P = 0.7746$). (J) Total distance (one-way ANOVA, $F(3, 12) = 0.8059$, $P = 0.9838$). (K) Representative images of hematoxylin and eosin (HE) staining in the brain among three group. the green arrows indicate pyknosis, and the red arrows signify obscured nuclear boundaries and increased cytoplasm. $^{*}P < 0.05$, $^{**}P < 0.01$ versus APP/PS1 group, $^{\#}P < 0.05$, $^{\#\#}P < 0.01$ versus WT group. TEM: transmission electron microscopy.

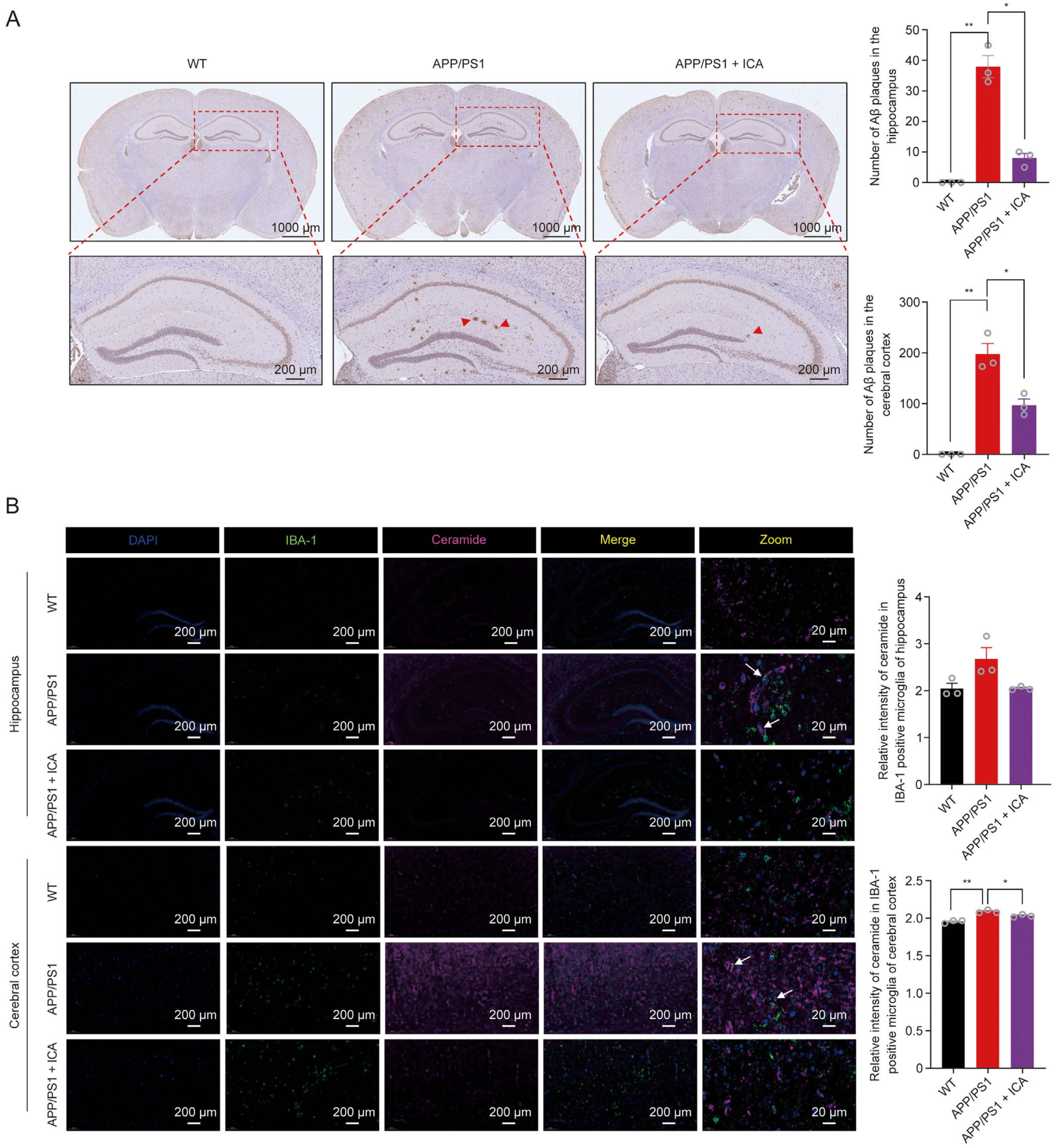

Fig. 8. Icariin (ICA) may improve cognitive dysfunction in amyloid precursor protein (APP)/presenilin 1 (PS1) mice by reducing amyloid beta (Aβ) deposition and cerebral ceramide (Cer) levels. (A) Representative Immunohistochemistry (IHC) images illustrate Aβ distribution in the brain among three groups (hippocampus: one-way analysis of variance (ANOVA), $F\,(3, 12) = 1.825$, $P < 0.0001$. Tukey's multiple comparisons test, APP/PS1 versus wild type (WT), $P < 0.0001$; APP/PS1 versus APP/PS1 + ICA, $P = 0.0002$; cortex: One-way ANOVA, $F\,(2, 6) = 0.9036$, $P = 0.0002$. Tukey's multiple comparisons test, APP/PS1 versus WT, $P = 0.0001$; APP/PS1 versus APP/PS1+ICA, $P = 0.0041$). (B) Representative immunofluorescent staining of Cer and ionized calcium-binding adaptor molecule 1 (IBA-1) in the brain among three group. Higher magnification images are presented (hippocampus: one-way ANOVA, $F\,(2, 6) = 0.5736$, $P = 0.0460$; cerebral cortex: one-way ANOVA, $F\,(2, 6) = 0.0007694$, $P = 0.0006$. Tukey's multiple comparisons test, APP/PS1 versus WT, $P = 0.0004$; APP/PS1 versus APP/PS1 + ICA, $P = 0.0270$). $^{*}P < 0.05$, $^{**}P < 0.01$ versus APP/PS1 group. DAPI: 4′,6-diamidino-2-phenylindole.

type-specific processes, in the human AD brain [10]. Moreover, research indicates that Aβ can directly induce neuronal pyroptosis through the caspase-1-GSDMD in APP/PS1 mice [35]. Another study found that Aβ42 induces astrocyte pyroptosis dependent on the GSDMD/GSDME/Caspase 11/NLRP3 pathway [36]. In summary, we hypothesize that widespread pyroptosis occurs in the AD brain and plays a critical role in AD pathology. However, it remains unclear whether Cer can induce or exacerbate pyroptosis or other

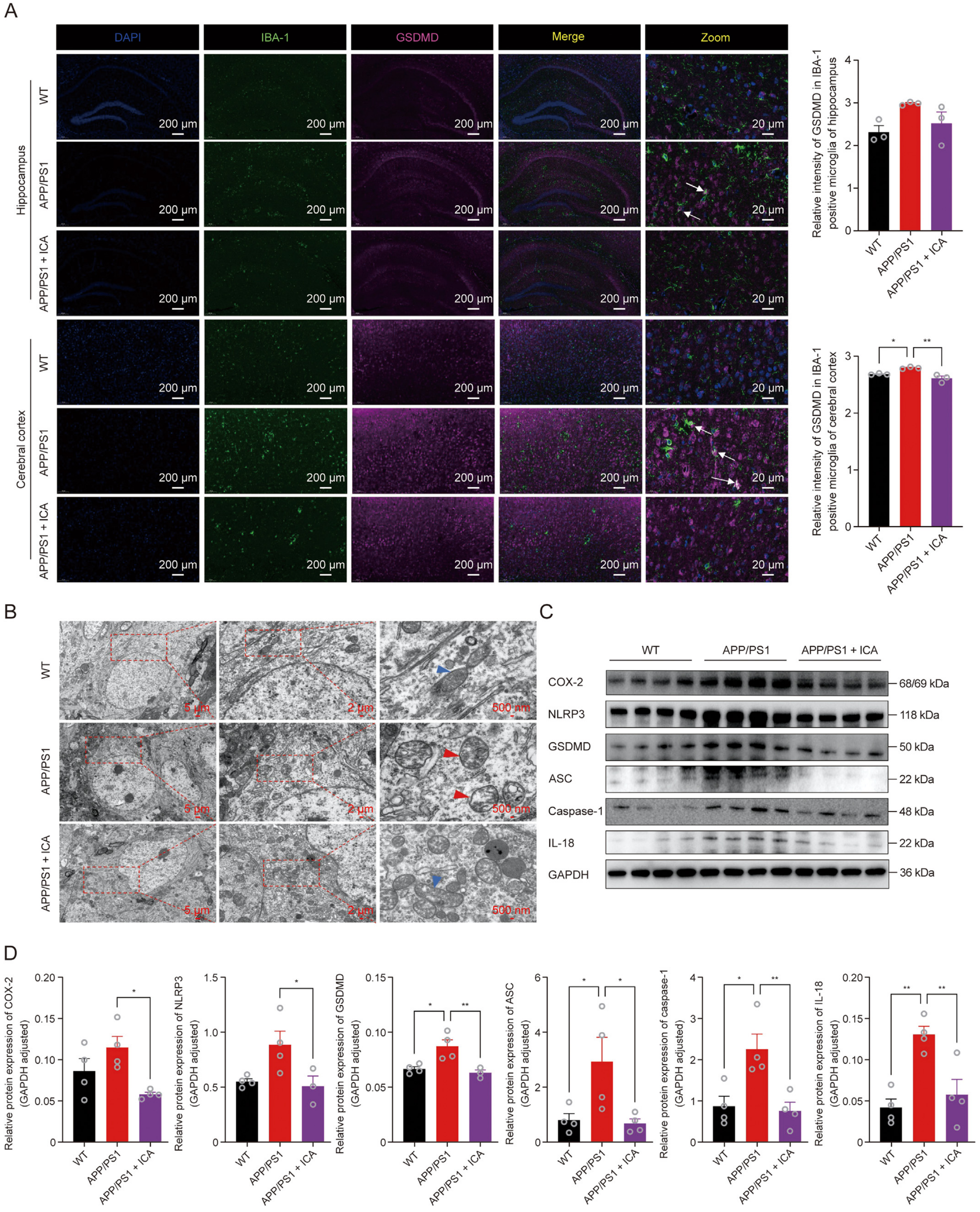

Fig. 9. Icariin (ICA) may improve cognitive dysfunction in amyloid precursor protein (APP)/presenilin 1 (PS1) mice by inhibiting microglial pyroptosis. (A) Representative immunofluorescent staining of gasdermin D (GSDMD) and ionized calcium-binding adaptor molecule 1 (IBA-1) in the brain among three group. Higher magnification images are presented (hippocampus: one-way analysis of variance (ANOVA), *F* (2, 6) = 1.098, *P* = 0.0911; cerebral cortex: one-way ANOVA, *F* (2, 6) = 1.571, *P* = 0.0055. Tukey's multiple comparisons test, APP/PS1 versus wild type (WT), *P* = 0.0367; APP/PS1 versus APP/PS1 + ICA, *P* = 0.0034). (B) Representative transmission electron microscopy (TEM) images

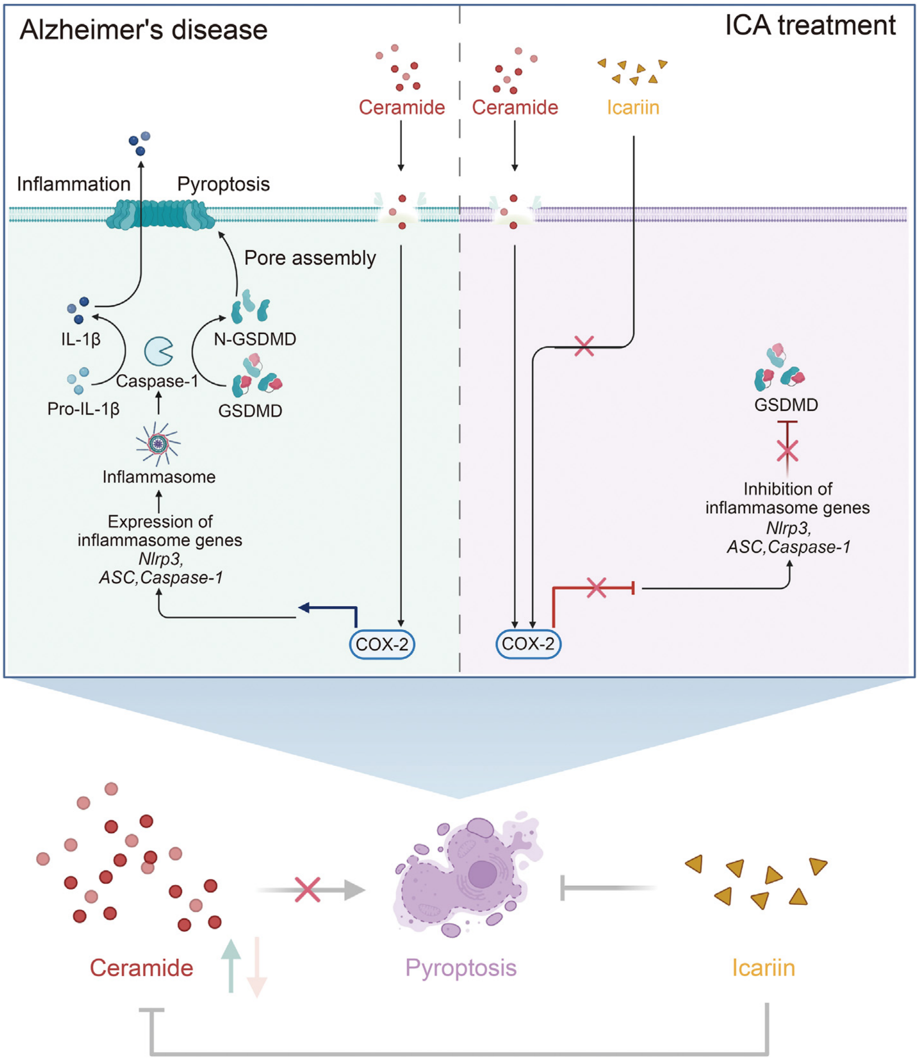

Fig. 10. A schematic diagram illustrating the occurrence of microglial pyroptosis and the protective effects of icariin (ICA) on ceramide (Cer)-induced microglia pyroptosis. Elevated Cer levels stimulate microglial cells, triggering the cyclooxygenase-2 (COX-2)/NOD-like receptor family, pyrin domain containing 3 (NLRP3) inflammasome/gasdermin D (GSDMD) signaling pathway, leading to increased inflammation, cell membrane rupture, and the occurrence of pyroptosis. ICA treatment can inhibit pyroptosis by reducing Cer levels and targeting COX-2.ASC: apoptosis-associated speck-like protein containing a caspase recruitment domain; IL-1β: interleukin-1β.

pathological changes in neurons and astrocytes, in addition to microglia. This will be a focus of our future research.

Interestingly, alongside the cognitive impairments and microglial pyroptosis in APP/PS1 mice, an increase in Cer levels within microglia was observed. Cers are elevated in the brain tissues, plasma, and cerebrospinal fluid (CSF) of AD patients and have been implicated in dysregulating autophagy, impairing mitochondrial health, and inducing cellular senescence [37]. Studies on human AD brains, as well as research into the oxidative stress induced by Aβ, suggest that dysregulated Cer production exacerbates neuronal dysfunction and death [38]. Furthermore, in brain tissues from patients with frontotemporal dementia and Pick's disease, Cer levels are elevated in association with astrocytes and are hypothesized to exert pro-inflammatory effects [39]. Reactive astrocytes release extracellular vesicles enriched in Cer that carry Aβ peptides [40]. Neurodegenerative diseases and aging have a direct connection with oxidative stress, which stimulates sphingomyelinase (SMase) activity, consequently elevating intracellular Cer concentration in neurons and oligodendrocytes [41]. Of particular interest is the ability of Cers to trigger pyroptosis, as demonstrated by a recent study showing Cer-

---

showing morphological changes of mitochondria. Higher magnification images are presented. Blue arrows indicating normal mitochondrial morphology, and red arrows indicating abnormal mitochondrial morphology, including rounded mitochondria, swelling, and blurred cristae. (C) The protein expression of cyclooxygenase-2 (COX-2), NOD-like receptor family, pyrin domain containing 3 (NLRP3), GSDMD, apoptosis-associated speck-like protein containing a caspase recruitment domain (ASC), caspase-1, and interleukin-18 (IL-18) in hippocampus was detected by Western blot assays. (D) Quantitative analysis of Western blot (COX-2: one-way ANOVA, $F(2, 9) = 3.492$, $P = 0.0257$. Tukey's multiple comparisons test, APP/PS1 versus WT, $P = 0.2094$; APP/PS1 versus APP/PS1 + ICA, $P = 0.0152$; NLRP3: one-way ANOVA, $F(2, 8) = 1.825$, $P = 0.0370$. Tukey's multiple comparisons test, APP/PS1 versus WT, $P = 0.0507$; APP/PS1 versus APP/PS1+ICA, $P = 0.0418$; GSDMD: one-way ANOVA, $F(2, 8) = 6.558$, $P = 0.0078$. Tukey's multiple comparisons test, APP/PS1 versus WT, $P = 0.0138$; APP/PS1 versus APP/PS1 + ICA, $P = 0.0087$; ASC: one-way ANOVA, $F(2, 9) = 15.23$, $P = 0.0289$. Tukey's multiple comparisons test, APP/PS1 versus WT, $P = 0.0398$; APP/PS1 versus APP/PS1 + ICA, $P = 0.0305$; caspase-1: one-way ANOVA, $F(2, 9) = 0.1516$, $P = 0.0079$. Tukey's multiple comparisons test, APP/PS1 versus WT, $P = 0.0131$; APP/PS1 versus APP/PS1 + ICA, $P = 0.0084$; IL-18: one-way ANOVA, $F(2, 9) = 0.3374$, $P = 0.0029$. Tukey's multiple comparisons test, APP/PS1 versus WT, $P = 0.0025$; APP/PS1 versus APP/PS1 + ICA, $P = 0.0080$). $^{*}P < 0.05$, $^{**}P < 0.01$ versus APP/PS1 group. GAPDH: glyceraldehyde-3-phosphate dehydrogenase.

induced pyroptosis through the TXNIP/NLRP3/GSDMD pathway in human umbilical vein endothelial cells [18]. However, the specific impact of elevated Cer levels on microglia in AD has been less explored. While recent studies have underscored the role of Cer in activating NLRP3 within microglia [15], it remains unclear whether the process of Cer regulating NLRP3 inflammasome leading to microglial pyroptosis involves other proteins. Our findings reveal COX-2's involvement in Cer-mediated NLRP3 inflammasome activation in microglial pyroptosis. Cers are reported to activate COX-2, promoting apoptosis under stress conditions [42]. Additionally, COX-2 is known to positively regulate NLRP3 inflammasome activation [15]. Therefore, it is hypothesized that Cer may exacerbate cognitive dysfunction by regulating COX-2-NLRP3 inflammasome-GSDMD axis, thereby inducing microglia pyroptosis.

Emerging evidence underscores the significant role of ICA in preventing AD development through various molecular mechanisms [43]. It has been reported that ICA modulates neurotransmitter levels, ameliorates mitochondrial and synaptic dysfunction, participates in anti-inflammatory and anti-apoptotic pathways, and addresses the primary pathological features of AD [44]. Our previous study revealed that ICA exerts its anti-AD effects by reducing various Cer levels in the gut of APP/PS1 mice [20]. Additionally, ICA has been found to possess anti-pyroptotic properties. For example, ICA alleviates hemorrhage shock and resuscitation-induced cognitive dysfunction and astrocytic pyroptosis in mice [22]. It has also been shown to inhibit NLRP3/caspase-1 signaling-mediated pyroptosis in osteoarthritis models, both *in vitro* and *in vivo* [23]. Moreover, ICA can suppress COX-2 protein expression in a dose-dependent manner, thereby attenuating lipopolysaccharide-induced microglial activation [45]. Research has further demonstrated that ICA reduces COX-2 expression levels across various inflammatory diseases and central nervous system disorders, including murine lupus nephritis, neuroinflammation, and Parkinson's Disease. Consistent with our findings, molecular docking, molecular dynamics, and CETSA results suggest that ICA may inhibit COX-2 levels by directly targeting COX-2, subsequently suppressing the NLRP3 inflammasome-GSDMD pathway and preventing microglial pyroptosis. In summary, we demonstrate for the first time that ICA not only reduces Cer levels in brain microglia but also inhibits the activation of the COX-2-NLRP3-GSDMD signaling pathway induced by Cer, thereby preventing microglial cell pyroptosis.

The cerebral cortex has garnered significant attention from researchers due to its critical role in spatial navigation and memory [46]. Its anatomical connectivity suggests that it functions as an interface between the anterior thalamic nuclei, entorhinal and parietal cortex, subiculum, and hippocampus, thereby supporting these cognitive processes [47]. Additionally, alterations in the cerebral cortex have been associated with the early stages of dementia and cognitive decline [48]. This aligns with our research findings. For example, our IF staining experiments for GSDMD and ceramide revealed that these changes were more pronounced in the cortex than in the hippocampus. In future studies, we will comprehensively investigate the roles and interactions of various brain regions in AD, rather than focusing on a single brain area.

While this study meticulously explores the pathogenic role of Cer in AD and the therapeutic effects of ICA, several limitations warrant mention. Primarily, we did not perform *in vitro* or *in vivo* experiments involving COX-2 knockdown or overexpression. In future research, we plan to develop COX-2 knockout and overexpression AD animal models to further clarify its critical role in AD. Additionally, the use of C2-Cer based on literature suggesting its ability to re-acylate into various Cer species, thus mimicking the pathological changes observed *in vivo* [49]. Considering the diverse types of Cers in biological systems, further investigations into different Cer types, such as C16 or C18-Cer, and their impacts on microglial cells or other brain cell types are essential. Moreover, despite preliminary evidence suggests that COX-2 is a target of ICA, further studies are necessary to explore the binding forms between ICA and COX-2, employing methods such as through co-immunoprecipitation (co-IP), pull-down assays, surface plasmon resonance (SPR), and co-crystallization experiments. Additionally, ICA may have other potential targets that require further investigation using methods like thermal proteome profiling (TPP), solvent-induced protein precipitation (SIP), and human proteome microarrays. Furthermore, while this research utilized APP/PS1 transgenic mice, other AD model mice should also be considered in future studies. The exact mechanisms by which ICA modulates Cer levels remain to be clarified, potentially involving metabolic enzymes or interactions with the gut microbiome.

5. Conclusion

In conclusion, our study provides significant insights into the pathological role of Cer in AD and introduced ICA as an innovative therapeutic intervention. We have demonstrated that elevated Cer levels are closely linked with cognitive decline in APP/PS1 mice, primarily through the activation of the COX-2, which further stimulates the NLRP3 inflammasome/GSDMD pathway, leading to microglial pyroptosis. Importantly, our findings suggest that ICA effectively improve AD pathology by reducing Cer levels and regulating the COX2-NLRP3 inflammasome-GSDMD axis, thus alleviating microglial pyroptosis. Through delineating these mechanisms, our research contributes to a deeper understanding of AD and opens avenues for the development of innovative treatment strategies aimed at modulating Cer levels and their pathological consequences.

CRediT authorship contribution statement

Hongli Li: Writing – original draft. **Qiao Xiao:** Methodology. **Lemei Zhu:** Project administration. **Jin Kang:** Formal analysis. **Qiong Zhan:** Supervision, Software, Project administration. **Weijun Peng:** Writing – review & editing, Funding acquisition.

Declaration of competing interest

The authors declare that there are no conflicts of interest.

Acknowledgments

This work was financially supported by the National Natural Science Foundation of China (Grant No.: 82374552), Hunan Provincial Natural Science Foundation of China for Distinguished Young Scholars (Grant No.: 2024JJ2086), The Science and Technology Innovation Program of Hunan Province, China (Grant No.: 2022RC1220), and Support Plan for High-level Health and Medical Talents in Hunan Province, China.

References

[1] J. Jia, Y. Ning, M. Chen, et al., Biomarker changes during 20 years preceding Alzheimer's disease, N. Engl. J. Med. 390 (2024) 712–722.
[2] E.E. Congdon, C. Ji, A.M. Tetlow, et al., Tau-targeting therapies for Alzheimer disease: Current status and future directions, Nat. Rev. Neurol. 19 (2023) 715–736.
[3] R. Kosoy, J.F. Fullard, B. Zeng, et al., Genetics of the human microglia regulome refines Alzheimer's disease risk loci, Nat. Genet. 54 (2022) 1145–1154.
[4] D. Singh, Astrocytic and microglial cells as the modulators of neuroinflammation in Alzheimer's disease, J. Neuroinflammation 19 (2022), 206.
[5] Z. Gao, K. Luo, Y. Hu, et al., Melatonin alleviates chronic stress-induced hippocampal microglia pyroptosis and subsequent depression-like behaviors by inhibiting Cathepsin B/NLRP3 signaling pathway in rats, Transl. Psychiatry 14 (2024), 166.

[6] Z. Yin, S. Herron, S. Silveira, et al., Identification of a protective microglial state mediated by miR-155 and interferon-γ signaling in a mouse model of Alzheimer's disease, Nat. Neurosci. 26 (2023) 1196−1207.

[7] Y. Zhou, Y. Zhang, H. Wang, et al., Microglial pyroptosis in hippocampus mediates sevolfurane-induced cognitive impairment in aged mice via ROS-NLRP3 inflammasome pathway, Int. Immunopharm. 116 (2023), 109725.

[8] G. Jing, J. Zuo, Q. Fang, et al., Erbin protects against sepsis-associated encephalopathy by attenuating microglia pyroptosis via IRE1α/Xbp1s-Ca2+ axis, J. Neuroinflammation 19 (2022), 237.

[9] X. Huang, C. Ye, X. Zhao, et al., TRIM45 aggravates microglia pyroptosis via Atg 5/NLRP3 axis in septic encephalopathy, J. Neuroinflammation 20 (2023), 284.

[10] S. Moonen, M.J. Koper, E. Van Schoor, et al., Pyroptosis in Alzheimer's disease: Cell type-specific activation in microglia, astrocytes and neurons, Acta Neuropathol. 145 (2023) 175−195.

[11] A.G. York, M.H. Skadow, J. Oh, et al., IL-10 constrains sphingolipid metabolism to limit inflammation, Nature 627 (2024) 628−635.

[12] S.M. Crivelli, C. Giovagnoni, L. Visseren, et al., Sphingolipids in Alzheimer's disease, how can we target them? Adv. Drug Deliv. Rev. 159 (2020) 214−231.

[13] L.S. Kalinichenko, E. Gulbins, J. Kornhuber, et al., Sphingolipid control of cognitive functions in health and disease, Prog. Lipid Res. 86 (2022), 101162.

[14] M. Yi, C. Zhang, Z. Zhang, et al., Integrated metabolomic and lipidomic analysis reveals the neuroprotective mechanisms of Bushen Tiansui formula in an A β 1-42-induced rat model of Alzheimer's disease, Oxid. Med. Cell. Longev. 2020 (2020), 5243453.

[15] H. Scheiblich, A. Schlütter, D.T. Golenbock, et al., Activation of the NLRP3 inflammasome in microglia: The role of ceramide, J. Neurochem. 143 (2017) 534−550.

[16] M. Gaggini, R. Ndreu, E. Michelucci, et al., Ceramides as mediators of oxidative stress and inflammation in cardiometabolic disease, Int. J. Mol. Sci. 23 (2022), 2719.

[17] L. Su, Y. Chen, C. Huang, et al., Targeting Src reactivates pyroptosis to reverse chemoresistance in lung and pancreatic cancer models, Sci. Transl. Med. 15 (2023), eabl7895.

[18] F. Liu, Y. Zhang, Y. Shi, et al., Ceramide induces pyroptosis through TXNIP/NLRP3/GSDMD pathway in HUVECs, BMC Mol. Cell Biol. 23 (2022), 54.

[19] G. Wang, X. Li, N. Li, et al., Icariin alleviates uveitis by targeting peroxiredoxin 3 to modulate retinal microglia M1/M2 phenotypic polarization, Redox Biol. 52 (2022), 102297.

[20] Y. Liu, H. Li, X. Wang, et al., Anti-Alzheimers molecular mechanism of icariin: Insights from gut microbiota, metabolomics, and network pharmacology, J. Transl. Med. 21 (2023), 277.

[21] Y. Wang, T. Zhu, M. Wang, et al., Icariin attenuates M1 activation of microglia and aβ plaque accumulation in the hippocampus and prefrontal cortex by up-regulating PPARγ in restraint/isolation-stressed APP/PS1 mice, Front. Neurosci. 13 (2019), 291.

[22] L. Zhang, R. Song, Y. Shan, et al., Effects of icariin on cognitive function and astrocytic pyroptosis in hemorrhagic shock resuscitation model mice, Chin. J. Behav. Med. & Brain Sci. (2023) 104−110.

[23] Y. Zu, Y. Mu, Q. Li, et al., Icariin alleviates osteoarthritis by inhibiting NLRP3-mediated pyroptosis, J. Orthop. Surg. Res. 14 (2019), 307.

[24] H. Li, Y. Tan, X. Cheng, et al., Untargeted metabolomics analysis of the hippocampus and cerebral cortex identified the neuroprotective mechanisms of Bushen Tiansui formula in an aβ25-35-induced rat model of Alzheimer's disease, Front. Pharmacol. 13 (2022), 990307.

[25] H. Wang, W. Yang, L. Xu, et al., BV2 membrane-coated PEGylated-liposomes delivered hFGF21 to cortical and hippocampal microglia for Alzheimer's disease therapy, Adv. Healthcare Mater. (2024), e2400125.

[26] E. Araki, C. Forster, J.M. Dubinsky, et al., Cyclooxygenase-2 inhibitor ns-398 protects neuronal cultures from lipopolysaccharide-induced neurotoxicity, Stroke 32 (2001) 2370−2375.

[27] T. Joki, O. Heese, D.C. Nikas, et al., Expression of cyclooxygenase 2 (COX-2) in human glioma and in vitro inhibition by a specific COX-2 inhibitor, NS-398, Cancer Res. 60 (2000) 4926−4931.

[28] C.S.-C. Biology, S. Abdulla, B. Aevermann, et al., CZ CELLxGENE discover: A single-cell data platform for scalable exploration, analysis and modeling of aggregated data, bioRxiv (2023-10), https://doi.org/10.1101/2023.10.30.563174.

[29] T. Li, R. Guo, Q. Zong, et al., Application of molecular docking in elaborating molecular mechanisms and interactions of supramolecular cyclodextrin, Carbohydr. Polym. 276 (2022), 118644.

[30] X. Zhang, W. Liu, J. Zan, et al., Untargeted lipidomics reveals progression of early Alzheimer's disease in APP/PS1 transgenic mice, Sci. Rep. 10 (2020), 14509.

[31] Y. Zhang, J. Zhang, Y. Zhao, et al., ChemR23 activation attenuates cognitive impairment in chronic cerebral hypoperfusion by inhibiting NLRP3 inflammasome-induced neuronal pyroptosis, Cell Death Dis. 14 (2023), 721.

[32] J. Zhou, J. Qiu, Y. Song, et al., Pyroptosis and degenerative diseases of the elderly, Cell Death Dis. 14 (2023), 94.

[33] Y. Huang, W. Xu, R. Zhou, NLRP3 inflammasome activation and cell death, Cell. Mol. Immunol. 18 (2021) 2114−2127.

[34] A. Litvinchuk, J.H. Suh, J.L. Guo, et al., Amelioration of Tau and ApoE4-linked glial lipid accumulation and neurodegeneration with an LXR agonist, Neuron 112 (2024), 2079.

[35] C. Han, Y. Yang, Q. Guan, et al., New mechanism of nerve injury in Alzheimer's disease: β-amyloid-induced neuronal pyroptosis, J. Cell Mol. Med. 24 (2020) 8078−8090.

[36] W. Hong, C. Hu, C. Wang, et al., Effects of amyloid β (Aβ)42 and Gasdermin D on the progression of Alzheimer's disease in vitro and in vivo through the regulation of astrocyte pyroptosis, Aging 15 (2023) 12209−12224.

[37] C. Tallon, B.J. Bell, M.M. Malvankar, et al., Inhibiting tau-induced elevated nSMase 2 activity and ceramides is therapeutic in an Alzheimer's disease mouse model, Transl. Neurodegener. 12 (2023), 56.

[38] R.G. Cutler, J. Kelly, K. Storie, et al., Involvement of oxidative stress-induced abnormalities in ceramide and cholesterol metabolism in brain aging and Alzheimer's disease, Proc. Natl. Acad. Sci. USA 101 (2004) 2070−2075.

[39] N.M. de Wit, S. den Hoedt, P. Martinez-Martinez, et al., Astrocytic ceramide as possible indicator of neuroinflammation, J. Neuroinflammation 16 (2019), 48.

[40] A. Elsherbini, A.S. Kirov, M.B. Dinkins, et al., Association of Aβ with ceramide-enriched astrosomes mediates Aβ neurotoxicity, Acta Neuropathol. Commun 8 (2020), 60.

[41] L.M. Pujol-Lereis, Alteration of sphingolipids in biofluids: Implications for neurodegenerative diseases, Int. J. Mol. Sci. 20 (2019), 3564.

[42] S.H. Park, J. Park, M. Lee, et al., Wheat ceramide powder mitigates ultraviolet B-induced oxidative stress and photoaging by inhibiting collagen proteolysis and promoting collagen synthesis in hairless mice, Prev. Nutr. Food Sci. 28 (2023) 418−426.

[43] L. Zheng, S. Wu, H. Jin, et al., Molecular mechanisms and therapeutic potential of icariin in the treatment of Alzheimer's disease, Phytomed. Int. J. Phytother. Phytopharm. 116 (2023), 154890.

[44] Z. Luo, J. Dong, J. Wu, Impact of Icariin and its derivatives on inflammatory diseases and relevant signaling pathways, Int. Immunopharm. 108 (2022), 108861.

[45] L. Yu, X. Dong, T. Huang, et al., Inhibition of ferroptosis by icariin treatment attenuates excessive ethanol consumption-induced atrial remodeling and susceptibility to atrial fibrillation, role of SIRT1, Apoptosis 28 (2023) 607−626.

[46] A. Steel, M.M. Billings, E.H. Silson, et al., A network linking scene perception and spatial memory systems in posterior cerebral cortex, Nat. Commun. 12 (2021), 2632.

[47] M. Stacho, D. Manahan-Vaughan, Mechanistic flexibility of the retrosplenial cortex enables its contribution to spatial cognition, Trends Neurosci. 45 (2022) 284−296.

[48] K.N.H. Dillen, H.I.L. Jacobs, J. Kukolja, et al., Aberrant functional connectivity differentiates retrosplenial cortex from posterior cingulate cortex in prodromal Alzheimer's disease, Neurobiol. Aging 44 (2016) 114−126.

[49] C.A. Vásquez-Londoño, M.J.R. Howes, G.M. Costa, et al., Scutellaria incarnata Vent. root extract and isolated phenylethanoid glycosides are neuroprotective against C2-ceramide toxicity, J. Ethnopharmacol. 307 (2023), 116218.